



**Politecnico  
di Torino**

**Politecnico di Torino**

**Facoltà di Ingegneria**

**Corso di Laurea Magistrale in Ingegneria Aerospaziale**

**Development of biodegradable air  
balloons for mini green radiosonde to  
measure fluctuations within warm  
clouds**

Thesis associated with the EU project H2020

**MSCA ITN ETN COMPLETE**

Relatrice:  
Prof.ssa Daniela Tordella

Candidato:  
Andrea Caporali

A.A. 2020/2021  
Sessione di Laurea di Ottobre 2021



# Abstract

Turbulent phenomena play a fundamental role in all of those microphysical processes that take place inside clouds and in the atmosphere in general. The tight connection between turbulence and clouds evolution, droplet generation and growth are still partly unknown nowadays. This lack of knowledge can be traced back to limited amount of information of in field data; obtaining these data is very complex because it implies the use of special radioprobe capable of floating passively, following the Lagrangian trajectory of the flow faithfully, without diverting either disturbing the stream. These reasons led to the birth of the COMPLETE project, a Horizon2020 programme, whose goal is to broaden the knowledge of the scientific community in the field of turbulence and its influence in clouds microphysical behaviour. A prototype of mini radiosonde, disposable, biodegradable and extra-light was designed and developed, capable of transmitting several data in real time to a ground receiver. The probe during the flight collects information about pressure, temperature, relative humidity, trajectory, wind speed, and sends it using an antenna at the ground station. In this thesis after illustrating the physics of clouds and its bond with turbulence are described the components of the probe and their functioning, the choice of the materials and their assembly, the data collected from the experiments in field and their analysis. In the end are exposed the reflections on the results achieved and possible future developments.

# Index

|   |    |
|---|----|
| <b>Chapter 1</b> .....  | 6  |
| Introduction .....  | 6  |
| <b>Chapter 2</b> .....  | 10 |
| Turbulence.....   | 10 |
| 2.1 Turbulence and the Closure Problem.....                   | 10 |
| 2.2 Turbulent Diffusion.....                                  | 12 |
| 2.3 Multi-Scales Theory of Turbulence .....                   | 17 |
| 2.3.1 The Energy Cascade .....                                | 18 |
| <b>Chapter 3</b> .....  | 22 |
| Clouds as source of uncertainty .....                         | 22 |
| 3.1 Clouds Classification .....                               | 23 |
| 3.2 Warm Clouds Formation.....                                | 26 |
| 3.2.1 Köhler equation .....                                   | 28 |
| 3.3 Cloud Droplet Diffusional Growth .....                    | 30 |
| 3.3.1 The two Modeling Methodologies .....                    | 32 |
| 3.3.2 Limitations of Modelling Methodologies.....             | 33 |
| 3.4 Activation and Growth of Droplets in Warm Clouds .....    | 34 |
| 3.4.1 CCN activation .....                                    | 34 |
| 3.4.2 Growth for diffusion/condensation of water vapour ..... | 35 |
| 3.4.3 Growth for collision/coalescence .....                  | 37 |
| 3.5 Clouds Microphysics.....                                  | 38 |
| 3.5.1 Impact of Turbulence on Cloud Microphysics.....         | 41 |
| 3.5.2 Air Turbulence and Droplet Interactions.....            | 41 |
| 3.5.3 Role of Turbulence in Droplets Motions.....             | 42 |
| 3.6 Entrainment and Large-Scale Mixing .....                  | 45 |
| 3.6.1 Mechanism of Entrainment .....                          | 46 |
| 3.6.2 Consequences of Entrainment .....                       | 47 |

|  |    |
|--|----|
| <b>Chapter 4</b> .....                         | 49 |
| The Radiosonde.....                            | 49 |
| 4.1 Mini-Radioprobe Structure .....            | 51 |
| 4.2 Characteristics of the Smart Material..... | 53 |
| 4.3 Working Principle .....                    | 55 |
| <b>Chapter 5</b> .....                         | 61 |
| Mater-Bi Air Balloon .....                     | 61 |
| 5.1 Preventive Estimations.....                | 62 |
| 5.2 Balloon size.....                          | 64 |
| 5.2.1 Balloon Assembly .....                   | 65 |
| 5.3 Procedure .....                            | 67 |
| <b>Chapter 6</b> .....                         | 70 |
| Data obtained from experiments .....           | 70 |
| 6.1 Levaldigi Experiments .....                | 70 |
| 6.2 INRiM Experiment .....                     | 76 |
| 6.3 INRiM Experiment #2 .....                  | 81 |
| <b>Chapter 7</b> .....                         | 86 |
| Conclusions and Future Developments.....       | 86 |
| <b>References</b> .....                        | 91 |

# Chapter 1

## Introduction

From the dawn of time the humankind has observed and investigated clouds and weather phenomena in general to understand and predict their behaviour. Knowing and eventually being able to foresee the weather and its evolutions has always been of crucial importance for life, to organize agriculture, to avoid disasters, floods or combat droughts.

Over the time, despite the technological evolution of instrumentation capable in atmospheric observations such as satellites, probes and meteorological stations. Clouds are a very complex environment where large scale are connected and influence the smaller ones and the other way round, even today in fact several physical and chemical phenomena which take place inside the clouds are mostly unknown, or at least only teorical concepts.

This lack of information and knowledge about clouds may have different reasons, the first one is the paucity of in-situ measurements along Lagrangian trajectories, which could provide very important information about the fluctuations of many physical and chemical quantities, from large to small scales.

The first one who paved the way for this type of experimentation was Lewis Fry Richardson (1881-1953), an English scientist whose contribution in different fields such as Mathematics and Meteorology is still nowadays extremely relevant. LFR's research between 1919 and 1926 led to great advances in understanding the special properties of

turbulent eddies and in providing a novel kind of physical explanation about their relationship with clouds development and evolution. [1]

During this period, he carried out several experiments to investigate material dispersion in the atmosphere due to turbulent eddies. Later he performed experiments with air balloons that travelled for many hours far away from the released point. Ticket attached to the balloons were brought back by people who found the balloons after they landed. This was fundamental because it allowed to plot the paths made during the flight, in correspondence of an increase of the distance travelled, there was an increase of dispersion between the balloons.

Two other experiments were held in 1929, which involved releasing seeds and small balloons simultaneously at different initial separations. Thanks to these LFR was able to derive the general law that the rate of increase of the square of the separation (the rate of diffusion  $K$ ) between objects diffusing in a turbulent flow grows proportionally to the relative distance raised to the power  $4/3$ , the famous “*four-thirds law*”. This showed conclusively that turbulence contains eddies with several length scales, and that different methods of analysis are necessary. Despite this many of the questions he raised in 1926 are still not answered, this is why his contribution is still extremely relevant today. [1]

For these reasons Horizon2020 Innovative Training Network Cloud-Micro Physics-Turbulence-Telemetry (MSCA-ITN-COMLETE) project was born. Its purpose is to develop a radioprobe able of floating in warm clouds and making measurements following Lagrangian trajectories, in fact the evaluation of turbulent dispersion can be done through the study of the relative position between the probes during the flight evaluated at different time instants. Moreover, the inability to retrieve the probe after the

launch means that it must be biodegradable, very cheap and simple to produce in several items [2].

It must have some fundamental characteristics such as transmitting data regarding its location (pressure, temperature, humidity, position, wind speed) in real time, to a ground receiver: it must therefore contain different types of sensors, a battery and electronic components capable of processing and sending the data. A further important objective is being able to follow Lagrangian trajectories, for this reason the probe must have reduced dimensions to reduce inertia and not being a disturb for the current: the diameter must not exceed 40cm and the materials used must be as light as possible. Finally, the radiosonde will be dispersed in the environment and not is reusable, so it must be very cheap, easy to produce in several units and, most important, biodegradable.

During the period I was involved in the COMPLETE project, I had the objective to work on the external structure of the mini radioprobe, my role was to design the air balloon and test after test try to improve it. I evaluated the necessary dimensions and weights to consent the probe to fluctuate passively at the right altitude; to follow with the greatest fidelity the Lagrangian trajectories the best shape is the sphere, so I tried to design a balloon as spherical as possible without compromising its structural strength; I managed to find a way to place the electronical components so that they affected the dynamics of the probe as little as possible.

In the next chapter of this thesis, an overview of current knowledge about turbulence is shown: most important characteristics, the complexity about its prediction, multi-scale theory and turbulent diffusion. The third chapter represent an investigation about clouds, their main characteristics, the influence of turbulence in their behaviour and development,

growth by condensation and collision of cloud droplets in a large- and small-scale turbulence, entrainment and detrainment in a turbulent environment. Chapter four accurately describes all the radioprobe components, the choice of the smart materials and the operating principle of the sonde. In the following chapter is the described my work in the laboratory, the design and development of the air balloon, the choice of the material to produce it the tools used and the steps for making it from scratch. Chapter six contains all the data analysed from the experiments made to prove the correct functioning of the radioprobe as a whole.

The results obtained from the tests highlight some determinants for which the radiosonde needs to be perfected but, nevertheless, confirm that the probe is able to collect information and transmit it, following the Lagrangian fluctuations of the current and is capable of working with other radioprobes simultaneously.

# Chapter 2

## Turbulence

In fluid dynamics turbulence or turbulent flow is a fluid motion characterized by sudden changes in pressure and flow velocity due to intense fluctuations. Most flow occurring in nature or in industrial applications are turbulent. Turbulence is a very complex and non-linear flow phenomenon; it contains vorticity which makes the flow rotational and difficult to predict, and no general theory to describe it exists.

Turbulent flow is space and time dependent with a very large number of spatial degrees of freedom, in fact the dynamics of turbulence involves all scales from the largest to the smallest. The different scales coexist superimposed in the flow with the smaller ones inside the larger ones. Energy is extracted from the mean flow by the large-scale motions and is transmitted down, through a process called “*energy cascade*”, at smaller scale until it is dissipated by viscous action at the smallest scale (*Kolmogorov scale*). The size of the large scales is generally determined by the environment in which the flow exist while the smallest dissipative scale is strictly related to the Reynolds number, the bigger it is, the smaller the scale is.

### 2.1 Turbulence and the Closure Problem

Turbulence is high Reynolds number fluid flow with both spatial and temporal disorder. In general, because of being so disordered, a turbulent flow has a wide range of scales, from the biggest to the smallest (Kolmogorov scale). The weather itself is an example of

turbulent flow, there are of course predictable aspects, we are in fact able to predict the average flow over an area or over a period of time, but in general is quite difficult to have detailed information in a short time frame.

We now suppose that in a flow, the velocity is given by a mean and a fluctuating component:

$$v = \bar{v} + v' \quad (\text{Equation 1})$$

This is known as *Reynolds decomposition*, where  $\bar{v}$  is the mean velocity field, and  $v'$  is the deviation or fluctuation. The mean might be a time average, in this case  $\bar{v}$  is a function of only space, or it might be a time mean over a finite period, or it might be some form of ensemble mean. The average of the fluctuation component is zero (by definition). We would like to predict the evolution of the mean flow  $\bar{v}$ , without predicting the evolution of the eddying flow and to do this we might substitute (equation 1) into the momentum equation and try to obtain a closed equation for the mean quantity  $\bar{v}$ . To keep algebra simply, for a model nonlinear system that obeys:

$$\frac{\partial u}{\partial t} + uu + ru = 0 \quad (\text{Equation 2})$$

The average of this equation is:

$$\frac{\partial \bar{u}}{\partial t} + \overline{uu} + r\bar{u} = 0 \quad (\text{Equation 3})$$

The value of the term  $\overline{uu}$  is not deducible simply by knowing  $\bar{u}$ , since it involves correlations between eddy quantities, namely  $\overline{u'u'}$ . That is,  $\overline{uu} = \bar{u}\bar{u} + \overline{u'u'} \neq \bar{u}\bar{u}$ . We can go to the next order to try to obtain an equation for  $\overline{uu}$ . First, we multiply (equation 2) by  $u$  to obtain an equation for  $u^2$ , and then average it to yield:

$$\frac{1}{2} \frac{\partial \overline{u^2}}{\partial t} + \overline{uuu} + r\overline{u^2} = 0 \quad (\text{Equation 4})$$

This equation contains the undetermined cubic term  $\overline{uuu}$ . An equation determining this would contain a quartic term, and so on in an unclosed hierarchy.

This same closure problem arises in the Navier-Stokes equations. If density is constant the x-momentum equation for an averaged flow is:

$$\frac{\partial \bar{u}}{\partial t} + (\bar{v} \cdot \nabla) \bar{u} = -\frac{\partial \bar{\Phi}}{\partial x} - \nabla \cdot \overline{v'u'} \quad (\text{Equation 5})$$

The last term, and the similar in the y- and z-equation, represent the effects of eddies on the mean flow and are known as *Reynolds stress tensor*.

The ‘closure problem’ of turbulence may be thought of as finding a representation of the Reynolds stresses in terms of mean flow quantities. Nobody has been able to usefully close the system without introducing a physical assumption not directly deducible from the equations of motion themselves. Indeed, it is not clear that a useful closed-form solution even exists [3].

## 2.2 Turbulent Diffusion

The statistics of two particles dispersion is historically the first issues which has been quantitatively addressed in the study of fully developed turbulence. This was done by Lewis Fry Richardson, in a pioneering work on the properties of dispersion in the atmosphere in 1926 [4].

Considering a cluster of  $N$  marked molecules that we can call  $A$  and defining a reference length,  $h$  for instance, we can build a grid formed by cells of dimensions  $h \times h$ . With  $A$  as

origin, we can count the number of marked molecules in each of these cells and at different time instance.  $A_{n,n+1}$  represent the number of particles in the cell between  $l=nh$  and  $l=(n+1)h$  where  $l$  is the distance from  $A$  and  $n$  is an integer. Now repeat the same process with every particle considered as the origin and using the same length range. The mean is:

$$Q_{n,n+1} = \frac{1}{N} (A_{n,n+1} + B_{n,n+1} + C_{n,n+1} + \dots) \quad (\text{Equation 6})$$

We obtain a set of quantities  $Q_{0,h}$ ,  $Q_{h,2h}$ ,  $Q_{2h,3h}$  ... which are the numbers of marked molecules per length, classified according to their distance  $l$  ( $0 - h$ ,  $h - 2h$ ,  $2h - 3h$ ...) from other molecules. Can be useful to represent a diagram in which the ordinate is  $Q$  and abscissa  $l$  (figure 2.1) [5].

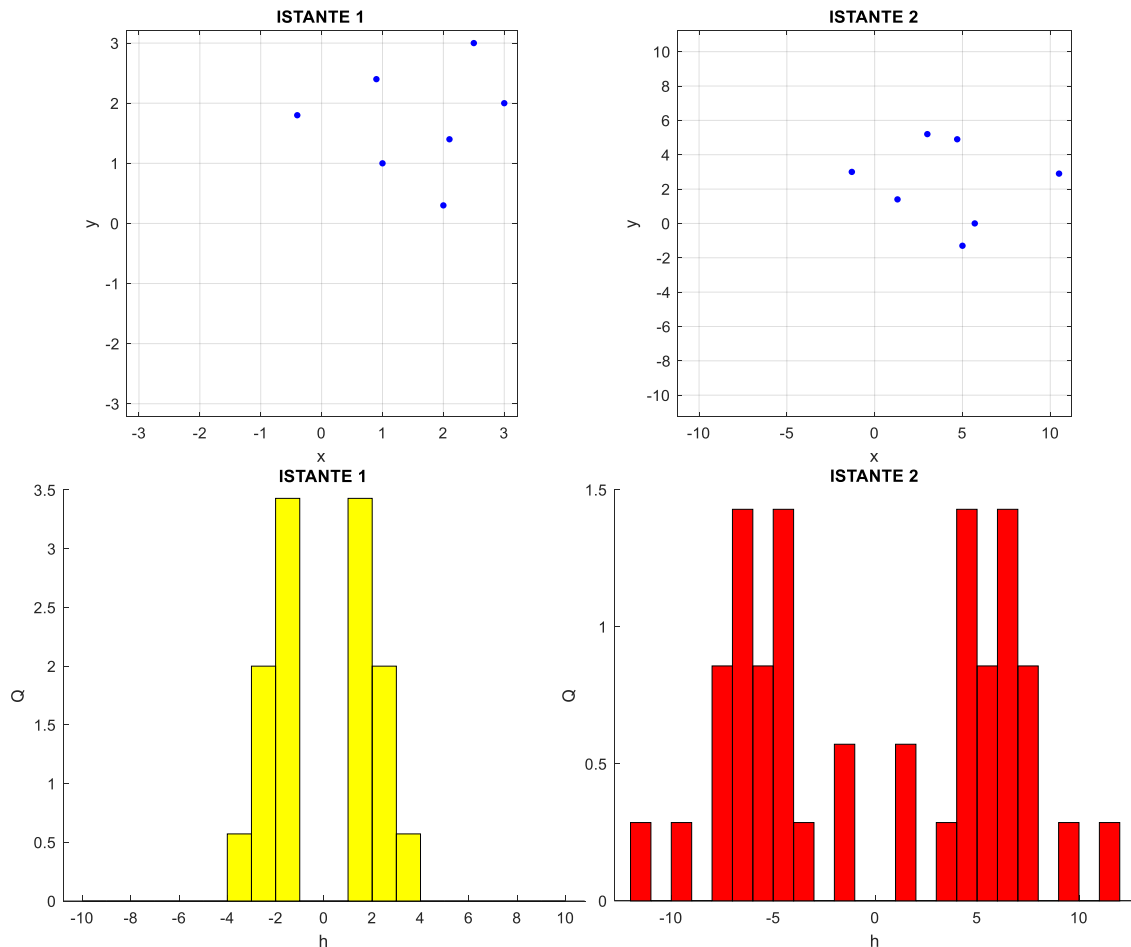


Figure 2.1: a) Distribution of the population of 7 molecules at two different time. b) Evolution of the number of neighbour  $Q$  at increasing length  $l$  considering a population of 7 molecules at two different time instances.

The unit of length  $h$  should be chosen so that in the average  $Q_{n,n+l}$  there is a considerable number of marked molecules, otherwise sampling errors might become important.

As we can see the  $(l, Q)$  diagram is symmetric about the  $Q$ -axis, in addition as diffusion proceed, the area subtended by the curve is constant, to do that the curve needs to flatten out step after step and this flattening is increased as  $l$  is greater. This means that some function of  $l$  which attains a limit as  $l \rightarrow \infty$  equal to that  $l \rightarrow -\infty$  exists. Then, we can say that  $Q$  must satisfy a differential equation like:

$$\frac{\partial Q}{\partial t} = \frac{\partial}{\partial l} \quad (\text{Equation 7})$$

At the final state we expect that the curve should be represented by a straight line parallel to the  $l$ -axis, which is confirmed by probability considerations.

Richardson's original description of relative dispersion is based on a diffusion equation for the probability density function of pair separation  $p(r,t)$  which can be written as:

$$\frac{\partial p(r,t)}{\partial t} = \frac{1}{r^2} \frac{\partial}{\partial r} r^2 K(r) \frac{\partial p(r,t)}{\partial r} \quad (\text{Equation 8})$$

The turbulent eddy diffusivity  $K$  was empirically determined by Richardson to follow the "four-thirds law"  $K(r) = k_0 \varepsilon^{1/3} r^{4/3}$ . The solution of (equation 6) for  $\delta$ -distribution initial condition has the form:

$$p(r, t) = \frac{A}{(k_0 t)^{3/2} \varepsilon} \exp\left(\frac{-9r^{2/3}}{4k_0 \varepsilon^{1/3} t}\right) \quad (\text{Equation 9})$$

The most peculiar feature of the Richardson distribution is non-Gaussianity with a very pronounced peak at the origin and fat tails. According to (equation 7) turbulent dispersion is self-similar in time. Relative dispersion can be defined as follow:

$$R^{2n}(t) \equiv C_{2n} \varepsilon^n t^{\alpha_{2n}} \quad (\text{Equation 10})$$

All the dimension-less coefficients  $C_{2n}$  are given in terms of the constant  $k_0$  and a single number, such as  $C_2$  is sufficient to parametrize turbulent dispersion. There is uncertainty about  $C_2$  values, anyway a recent experimental investigation gives the value  $C_2 = 0.55$  [4], [6].

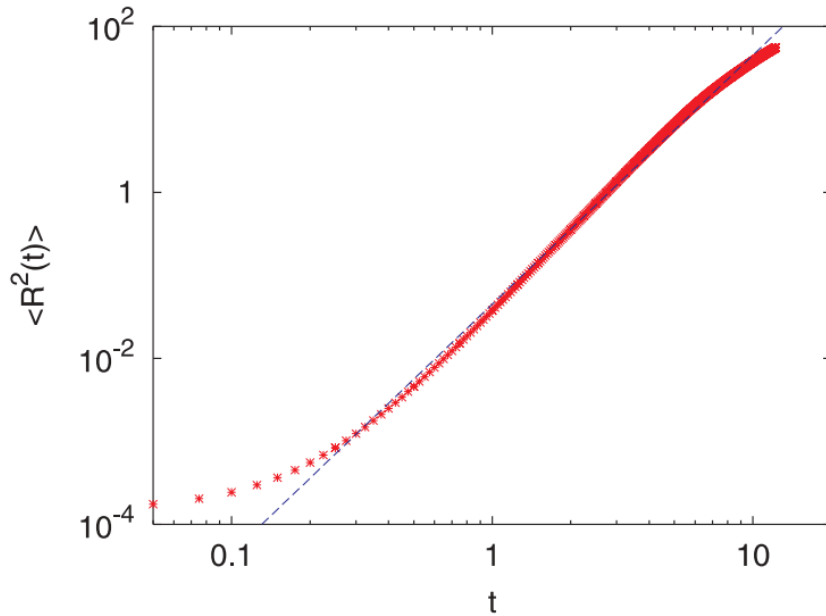


Figure 2.2: Relative dispersion  $R^2(t)$  versus time. The blue line is Richardson  $t^3$  law (equation 7).

The most widely used recipe to address the closure problem is by way of turbulent diffusion, or eddy diffusion. The idea comes by way of an analogy with molecular diffusion. Let us suppose that a fluid carries with it a tracer,  $\varphi$ , that satisfies an equation like:

$$\frac{D\varphi}{Dt} = k\nabla^2\varphi \quad (\text{Equation 11})$$

Where  $k$  is the molecular diffusivity. For simplicity we suppose that the flow is 2-dimensional and incompressible, and that the flow and the tracer have both a mean and a fluctuating component. The mean component of (equation 6) can be written as:

$$\frac{\partial \bar{\varphi}}{\partial t} + \frac{\partial \bar{u}\bar{\varphi}}{\partial x} + \frac{\partial \bar{v}\bar{\varphi}}{\partial y} = -\frac{\partial \overline{u'\varphi'}}{\partial x} - \frac{\partial \overline{v'\varphi'}}{\partial y} + k\nabla^2 \bar{\varphi} \quad (\text{Equation 12})$$

Now, consider a fluctuating parcel of fluid that, on average, carries its value of  $\varphi$  with it a certain distance  $l$ , a ‘mixing length’, before mixing with its surroundings. If there is a mean gradient of  $\varphi$  in the direction of movement (for example  $y$ -direction) then the value of  $\varphi'$  is given by:

$$\varphi' = -l \frac{\partial \varphi}{\partial y} \quad (\text{Equation 13})$$

If the dominant eddies have a typical speed  $v'$  then the eddy transport is given by:

$$\overline{v'\varphi'} = -K \frac{\partial \bar{\varphi}}{\partial y} \quad (\text{Equation 14})$$

Where:

$$K = -\overline{v'l} \quad (\text{Equation 15})$$

In this expression,  $K$  is an eddy diffusivity, the product of the velocity and length scale of the dominant eddies of the system.

If we assume that the same process occurs in the  $x$ -direction we obtain:

$$\frac{\partial \bar{\varphi}}{\partial t} + \frac{\partial \bar{u}\bar{\varphi}}{\partial x} + \frac{\partial \bar{v}\bar{\varphi}}{\partial y} = K\nabla^2 \bar{\varphi} + k\nabla^2 \bar{\varphi} \quad (\text{Equation 16})$$

In most turbulent flows the eddy diffusivity  $K$  is much larger than the molecular  $k$  because the mixing length is orders of magnitude larger than the corresponding molecular mixing

length, which is the average distance that a molecule goes before interacting with another molecule, also known as mean free path [5].

The presence of a molecular viscosity is important because it allows mixing to take place in the first instance; the turbulence amplifies the molecular mixing enormously, but that mixing must be present. Equation 11 is very useful for treating the enhanced transport associated with a turbulent flow. It says that if we are unable to explicitly model the small scales of a turbulent flow, then we might be able to approximately simulate the effects of the small scales using a turbulent diffusion [3].

### 2.3 Multi-Scales Theory of Turbulence

One theory that find many feedback in several experiments is the spectral theory of Kolmogorov, proposed in 1941 and often known as *K41 Theory*. [7]

Suppose that we have a mixed fluid at large spatial scale,  $L_0$ , and we put energy into the fluid at that scale at a rate  $\varepsilon$ , where it has units of energy/(time  $\times$  mass), or  $[\text{m}^2 \text{s}^{-3}]$ . This energized fluid becomes turbulent, creating scales of motion much smaller than  $L_0$ . In other words, energy create a transfer of itself from bigger to smaller scales. This process continues until we come to a boundary condition in which the Reynolds number  $Re = \frac{UL_v}{\nu}$  is order one and the viscous effects are extremely significant.

For instance, if  $\nu = 1 \times 10^{-7} [\text{m}^2 \text{s}^{-1}]$  is the cinematic viscosity and  $U = 1 [\text{m s}^{-1}]$  then the viscous scale is given by [7]:

$$L_v \approx \frac{\nu}{U} = 10^{-7} [\text{m}] \quad (\text{Equation 17})$$

### 2.3.1 The Energy Cascade

We now suppose that the fluid is stirred at large scales and that this energy is transferred to smaller scales where it is dissipated by viscosity. This process, also known as '*energy cascade*', is typical of non-linear system, like turbulence itself.

Larger eddies, with a lot of energy, disintegrating itself, yield part of this kinetic energy to smaller scales. If the initial level of energy is high enough, then a wide range of different scales is created, and the process described above continues until is reached the smallest scale of the system at which inertial and viscous contributions are comparable [7].

The key assumption is to suppose that, if the forcing scale is sufficiently larger than the dissipation scale, there exists a range of scales that is intermediate between the large and the dissipation scales and where neither forcing nor dissipation are explicitly important to dynamics of the system. This assumption, known as '*locality hypothesis*', depends on the non-linear transfer of energy being sufficiently local. This intermediate range is called '*inertial range*'.

Now, we have no general theory for the energy spectrum of a turbulent fluid, but we might imagine it takes the general form:

$$E(k) = f(\varepsilon, k, k_0, k_\nu) \quad (\text{Equation 18})$$

where the right-hand side denotes a function of the spectral energy flux or cascade rate  $\varepsilon$ , the wavenumber  $k$ , the forcing wavenumber  $k_0$ , and the wavenumber at which dissipation acts.  $k_\nu$ . The locality hypothesis essentially says, that at some scale within the inertial range, the flux of energy to smaller scales depends only on process occurring at or near

that scale, then the energy flux is only a function of  $E$  and  $k$ , or equivalently that the energy spectrum can be a function only of the energy flux  $\varepsilon$  and the wavenumber itself.

The energy spectrum takes the form:

$$E(k) = g(\varepsilon, k) \quad (\text{Equation 19})$$

the function  $g$  is assumed to be universal, the same for every turbulent flow [3].

To understand the form of the function  $g$  we can use dimensional analysis. In (equation 14) the left-hand side has dimension  $L^3 / T^2$ ; the factor  $T^{-2}$  can only be balanced by  $\varepsilon^{2/3}$  because  $k$  has no time dependence; we obtain:

$$E(k) = \varepsilon^{2/3} g(k) \quad (\text{Equation 20})$$

$$\frac{L^3}{T^2} \sim \frac{L^3}{T^2} g(k) \quad (\text{Equation 21})$$

evidently  $g(k)$  must have the dimensions  $L^{5/3}$  and we finally obtain:

$$E(k) = K \varepsilon^{2/3} k^{-5/3} \quad (\text{Equation 22})$$

This equation represents the famous ‘Kolmogorov spectrum’ and it is shown in the figure below (figure 2.3). The parameter  $K$  is a dimension-less constant, it is known as Kolmogorov’s constant and experimentally its value is found to be about 1.5 [7].

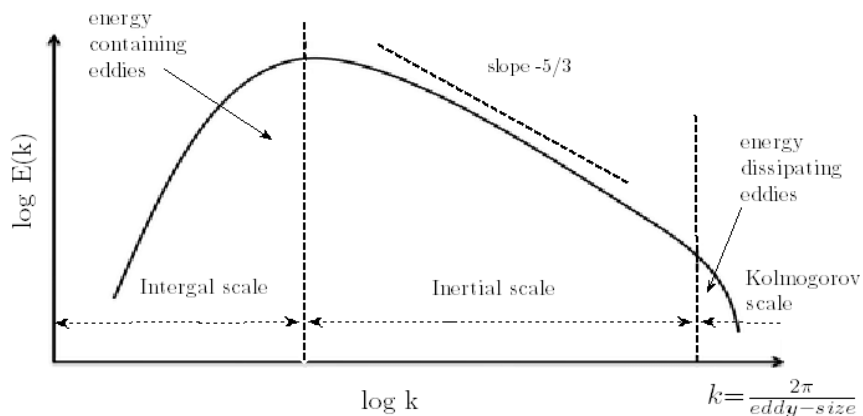


Figure 2.3: Energy spectrum in three-dimensional turbulence in Kolmogorov's Theory

As we said at some small length scale, we should expect viscosity to become important. In the inertial-range friction is unimportant because the time scales on which it acts are too long and the dynamic effects dominate. The viscous or dissipation time scale at a defined scale  $k$ , is:

$$\tau_k^v \sim \frac{1}{k^2 \nu} \quad (\text{Equation 23})$$

so that the viscous time scale decrease as in  $k$  increases and the length scale decreases.

The eddy turnover, or the inertial time scale in the Kolmogorov spectrum is:

$$\tau_k = \varepsilon^{-1/3} k^{-2/3} \quad (\text{Equation 24})$$

the wavenumber at which dissipation become significative is given by comparing the two equations above:

$$k_v \sim \left(\frac{\varepsilon}{\nu^3}\right)^{1/4} \quad (\text{Equation 25})$$

$$\eta \sim \left(\frac{\nu^3}{\varepsilon}\right)^{1/4} \quad (\text{Equation 26})$$

where  $\eta$  is called the *Kolmogorov scale*. It can be defined as the smallest scale in a turbulent flow, where the viscous effects are dominant, and the turbulent kinetic energy is dissipated into heat [8].

The Kolmogorov scale is achieved when inertial effects can be compared with viscous effects, which means that Reynolds number is about one.

An interesting consequence of the theory is that the rate of energy dissipation by viscous effects is independent of the magnitude of the viscosity coefficient. This might seem strange, in fact if the viscosity is smaller, we may think that there must be less

dissipation, but this is not what happen. If we reduce the viscosity, the cascade proceeds to smaller scales but the total dissipation stays the same and it is equal to the energy input  $\varepsilon$  at the level of the larger eddies. So, dissipation take place at the end of the energy cascade process and the rate of dissipation  $\varepsilon$  is determined by the first process in the sequence, which is the transfer of energy from the mean motion to the largest eddies and the consequent transfer to smaller eddies [3], [7].

# Chapter 3

## Clouds as source of uncertainty

Clouds are a complex environment and a key element in climate change and climate sensitivity, since their characteristics directly influence the global hydrological cycle (through precipitation), the radiation budget, and the various atmospheric dynamics [9].

With ever-increasing importance being placed on quantifiable predictions – from forecasting the local weather to anticipating climate change – we must understand how clouds influence and are connected with the atmosphere, and how they interact with anthropogenic pollutants or in general with human lifestyle [10].

Clouds systematic investigations took place only in the last century. At the beginning speculations about the composition and nature of clouds persisted for many years. Direct observations from balloons and aircraft are the most effective methods to develop a base of empirical knowledge upon which the research community could later build testable hypotheses. With ongoing improvements in instrumentation and measurement techniques, the invention of cloud chambers, and the ability to test hypotheses quantitatively, the research community has gradually expanded its knowledge and quantitative understanding of clouds [8].

The atmosphere, with all its dynamical and chemical complexity, is the environment in which clouds form. The atmosphere is a mixture of a huge number of chemical compounds, some of them gaseous, some particulate. Water represent only one of those myriad components, but the only one that changes phase under specific

conditions. The atmosphere is far more than “dry air” and water vapor, so any modern treatment of clouds must deal with this mixture head-on. Indeed, cloud droplets form on the more soluble subset of the particulate matter, and they subsequently absorb some of the trace gases. The micro-physical properties, even the macro-physical forms of clouds are significantly affected by the composition of the air, many of those chemicals are altered and removed from the atmosphere by clouds and the precipitation produced [8].

### 3.1 Clouds Classification

Several kinds of clouds exist in bibliography: due to the difficulty in distinguishing them, a simplified classification of most common cloud types is reported.

- *Stratiform clouds* (Figure 3.1) are the most stable type. This kind of cloud presents generally flat, sheet-like structures and it rarely produce precipitation. It is common to found them at every level of the troposphere and they usually do not produce precipitations [11].



*Figure 3.1: A sea of Stratiform cloud laps against the edge of Victoria Dandenong Ranges, Australia*

- *Cirriiform clouds* have a filament shape (Figure 3.2) and they are mostly stable. This kind of cloud is present only at high tropospheric altitudes and usually does not produce precipitations [11].



Figure 3.2: Picture of a Cirriiform Cloud.

- *Stratocumuliform clouds* (Figure 3.3) embody both stratiform and cumuliform characteristics. These clouds are generally stable, and precipitations depend on altitude at which the cloud is located [11].

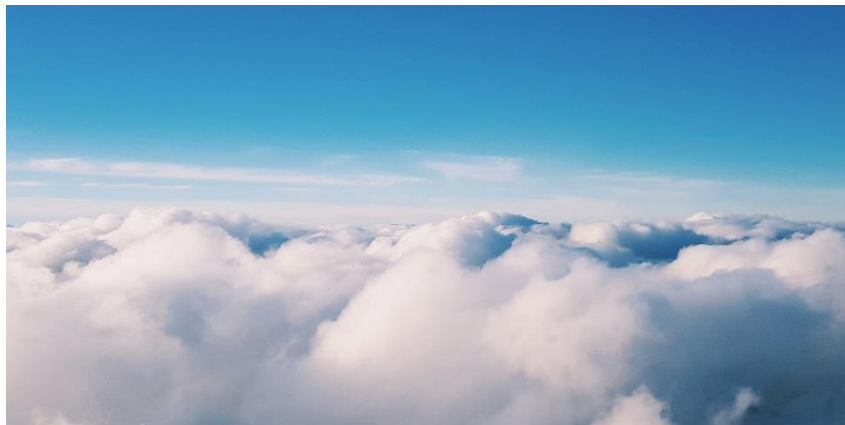


Figure 3.3: Picture taken of a Stratocumuliform Cloud.

- *Cumuliform clouds* (Figure 3.4) have greater instability as their dimension grow. This type of cloud has heaps or tufts shapes and might be low-level or multi-level (in this case precipitations remains abundant) [11].



Figure 3.4: Picture of a Cumulus Cloud

- *Cumulunimbiform clouds* (Figure 3.5) develop vertically. Are characterised by high turbulence and instability and can produce moderate to heavy rains [11].



Figure 3.5: Picture of a Cumulonimbus Cloud

## 3.2 Warm Clouds Formation

A typical warm cloud first develops as moist air rises, either by slow ascent in a synoptic-scale weather system or by rapid ascent during convection, beyond the thermodynamic cloud base (100% relative humidity). The early stages of cloud formation follow a common pattern regardless of the cause of uplift.

A defined amount of air is characterized by a mixing ratio, which is the content of water vapor (measured in g) per kilogram of dry air; this quantity can be also expressed not dimensionally as *relative humidity* [12]. Exists a maximum value of mixing ratio for which air becomes saturated and it is not able to contain more water vapor (relative humidity is 100%). Supersaturation is defined as the relative degree of watervapor pressure exceeding the saturation vapor pressure. From the moment that the air is supersaturated, formation of cloud takes place [12].

Consider the simplified scenario in which a parcel of moist air starts from near ground level and rises adiabatically at a constant rate. The consequences of this uplift are illustrated in the figure below (figure 3.6) [8].

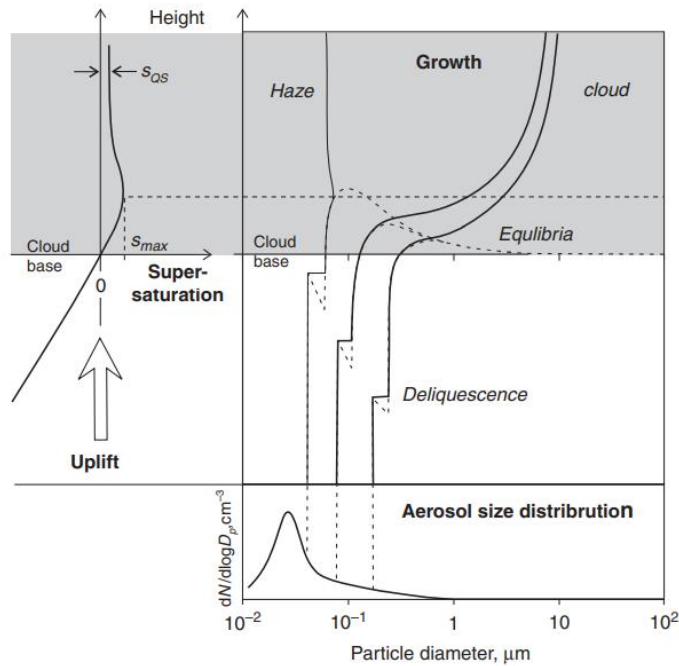


Figure 3.6: Evolution of the microphysical properties of a warm cloud during the adiabatic uplift of a moist air parcel. Left: Evolution of supersaturation as the parcel passes through cloud base. Right: Diameters of three representative particles as they grow from dry sizes (distribution shown at bottom) to aqueous solution droplets in response to the changing supersaturation.

The air is initially subsaturated and contains a population of dry aerosol particles distributed in size according to the curve shown near the bottom. Most of the particles have diameters close to  $0.02\mu\text{m}$ , but a significant number have larger diameters. Three representative sizes are shown by vertical lines that extend upward into the growth diagram above. As uplift proceeds, the relative humidity in the parcel increases, as shown on the left by the supersaturation curve becoming less negative. In response, the aerosol particles (assumed to be soluble) deliquesce and become liquid droplets. With continued uplift, the droplets grow by condensation and follow the Köhler-theory equilibrium curves. As the parcel passes through cloud base and the supersaturation becomes positive, large particles having small critical supersaturations activate first and grow rapidly beyond their respective critical sizes because the ambient supersaturation is larger than the respective equilibria. This growth behaviour is exemplified by the two bold curves

that separate away from the Köhler curves at their peaks. The uptake of vapor by the growth of the cloud droplets gradually depletes the excess vapor, which causes the supersaturation to reach a maximum value ( $s_{\max}$ ) and begin decreasing toward quasi-stationary values ( $s_{QS}$ ). Smaller aerosol particles, those having critical supersaturations larger than the maximum ambient supersaturation (exemplified by the light curve), grow slightly but are unable to activate (grow beyond the equilibrium maximum). These unactivated particles remain as small haze droplets [8].

### 3.2.1 Köhler equation

Hydrophilic particles (water loving) take on water as humidity increases and increase in size. Above a certain relative humidity soluble particle will deliquesce – the solid particle dissolves in the water it has taken on and becomes a tiny liquid drop, but not yet a cloud drop. For many soluble salts deliquescence happens at relative humidity around 60 – 80%.

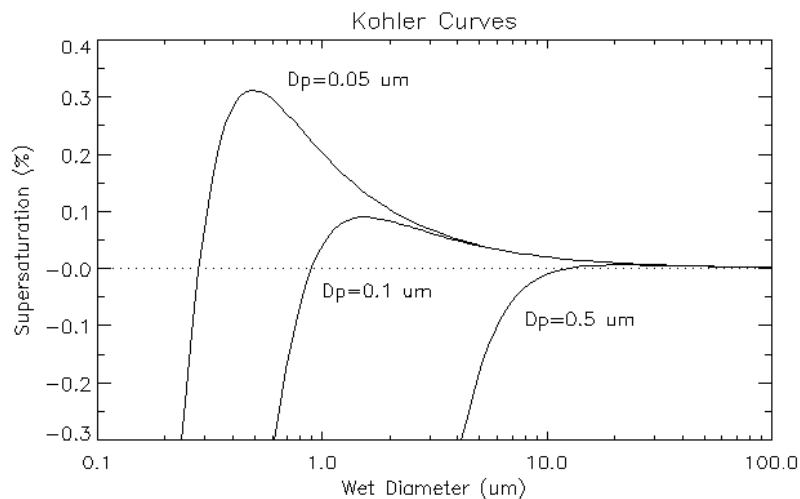


Figure 3.8: Köhler curves showing how the critical diameter and supersaturation are dependent upon the amount of solute. It is assumed here that the solute is a perfect sphere of sodium chloride.

These droplets exist in equilibrium with water vapour in the surrounding air. The growth of such particles with increase in relative humidity is expressed by the *Köhler equation* and is a function of the size and chemical composition of the particle.

$$\frac{e'}{e_s} = \left[ \exp \frac{2\sigma'}{n' kTr} \right] \left[ 1 + \frac{imM_w}{M_s \left( \frac{4}{3}\pi r^3 \rho' - m \right)} \right]^{-1} \quad (\text{Equation 27})$$

Where:

- $e'$  = vapour pressure of air adjacent to a droplet of given radius  $r$ .
- $\sigma'$  and  $n'$  = surface energy and number density of water molecules in the solution respectively
- $m$  = mass of salt dissolved in droplet
- $i$  = no. of ions each salt molecule dissociates into
- $M_s$  = molecular mass of salt and  $M_w$  = molecular mass of water.

As humidity increases, aerosol continues to swell, even after vapour saturation is reached. Once a critical supersaturation is reached, corresponding to the peak of the Köhler curve for that particle, a particle becomes activated as a cloud droplet. Activated particles are no longer in stable equilibrium with the vapour phase but can continue to grow by vapour deposition if conditions remain supersaturated.

Droplet size is determined by the number of particles activated and the amount of water vapour available for condensation which is generally determined by the vertical height of an adiabatic ascent. If droplets are able to grow to a sufficient size and the cloud exists for a sufficient length of time droplets will coalesce as they collide with each other through random motion, gravitational settling, or motion within the dynamics of the cloud

system. Through coalescence large droplets are produced. These large droplets have a larger gravitational settling velocity than smaller particles and begin to fall out of the cloud. In doing so they are moving more rapidly with respect to other cloud droplets, so the rate of coalescence increases, and precipitation drops are formed [13].

### **3.3 Cloud Droplet Diffusional Growth**

The problem of how cloud particles grow, whether water droplets or ice crystals, has attracted attention for many years [14].

Firstly, the growth rate of cloud particles by condensation or sublimation in a supersaturated environment decreases as the particles become larger, due to the reduced ratio of surface area to volume. This implies that even if the initial spectrum of sizes of cloud particles is broad, subsequent growth of the particles will lead to a narrowing of the spectrum as the mean size increases, provided all particles are exposed to the same supersaturation [7], [15].

The second difficulty in explaining droplet growth comes from the fact that the growth rate by coalescence in still air increases rapidly with particle size due to the increased terminal velocities and increased inertia of the particles; small droplets tend to follow the relative streamlines of the air flowing around a large droplet while larger droplets are less easily deflected. For water droplets falling in still air, growth by coalescence is very slow until some droplets have reached a radius in excess of 20  $\mu\text{m}$ , although subsequent growth to drizzle size may take only a few minutes in deep clouds with high values of liquid water content [7].

Estimations of droplet growth by condensation and coalescence in still air and assuming conditions appropriate to moderate cumulus clouds are shown in (figure 3.8).

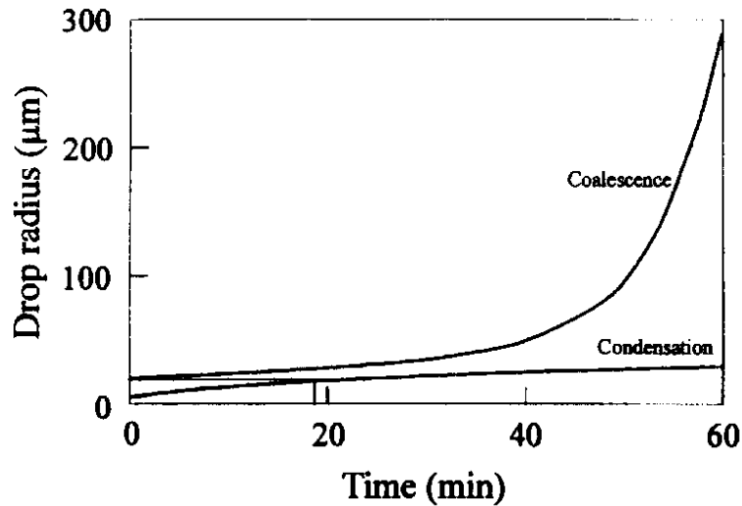


Figure 3.8: Estimated growth of droplets by condensation and coalescence under conditions appropriate to small cumulus.

The growth of a droplet from 10  $\mu\text{m}$  radius to 20  $\mu\text{m}$  by condensation at a supersaturation of 0.2% takes almost 20 min while growth by coalescence from 20  $\mu\text{m}$  to drizzle drop size ( $\sim 100 \mu\text{m}$ ) in a cloud with a liquid water content of  $1 \text{ g m}^{-3}$  would take around 1h [15]. It should be noted that this calculation of growth by coalescence underestimates the growth time since it assumes that a drop coalesces with all of the smaller droplets lying in its path. The combined growth time is much greater than the lifetime of many small precipitating cumulus clouds. It is also evident from this figure that droplets cannot grow to drizzle drop size by condensation alone [7].

### 3.3.1 The two Modeling Methodologies

When a simulation of the droplet spectral shape is required, there are two basic modelling methodologies that can be used.

The first one is a traditional bin approach where the Eulerian spectral density function that is continuous in space and time is used. In its numerical implementation, the spectral density function is represented by a finite number of radius (or mass) bins. Each bin is advected in the physical space, and all bins are combined at model grid locations to calculate the change in the spectral density function due to droplet growth [16].

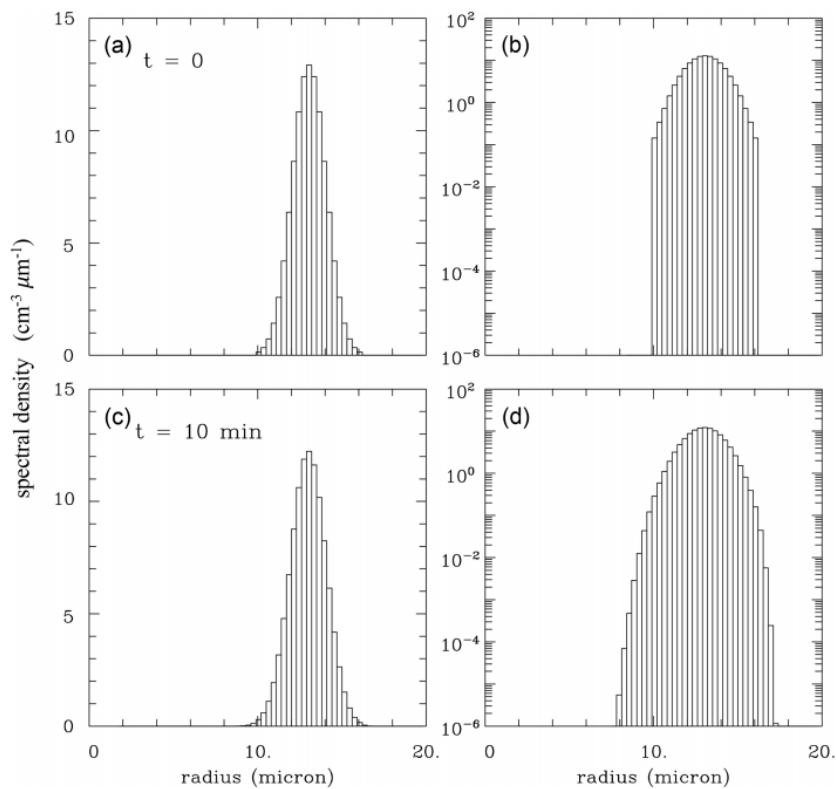


Figure 3.9: Initial droplet spectra (a, b) and spectra at the time of 10 min (c, d) for bin simulations. Panels (a, c) and (b, d) show spectra using a linear and logarithmic vertical scale, respectively.

The second approach represents the multiphase nature of real clouds by applying Lagrangian point particles. Each particle represents an ensemble of natural droplets with

the same properties, it is advected by the simulated air flow, and it grows in response to local conditions. The Lagrangian approach is a relatively novel modeling technique that is gaining popularity in cloud modeling because of its fidelity, especially for the simulation of aerosol–cloud interactions [16].

### **3.3.2 Limitations of Modelling Methodologies**

The two methodologies have their inherent limitations. The bin microphysics are affected by the numerical diffusion as any Eulerian approach. Advection of bins in the physical space typically leads to unavoidable numerical spreading of regions with rapid droplet spectral changes, for instance, near cloud edges [17].

For the Lagrangian microphysics, an obvious limitation is the limited and usually small number of Lagrangian particles that can be afforded in realistic cloud simulations, especially considering an enormous number of cloud and precipitation particles in natural clouds. However, the Lagrangian methodology has clear benefits when compared to the bin scheme [7]. These include the lack of numerical diffusion, the realistic representation of the stochastic nature of the cloud droplet growth, the possibility of including a physically based representation of the unresolved scales' impact on droplet growth (i.e., allowing the multiscale simulation of a turbulent cloud), and the provision of a better framework for aerosol–cloud interactions and the representation of ice processes [16].

### **3.4 Activation and Growth of Droplets in Warm Clouds**

Warm clouds droplets activation and growth up to raindrop size take place through three fundamental steps:

- CCN activation.
- Growth for diffusion/condensation of water vapour.
- Growth for collision/coalescence.

#### **3.4.1 CCN activation**

CCNs (Cloud Condensation Nuclei) are atmospheric aerosols of some micron, originated by micro-particles deeply hygroscopic on which water vapor tends to condensate [18],[19].

The number of CCN is directly connected with supersaturation, once enough CCN are activated, the supersaturation begins to decrease (figure 3.12), and CCN activation is complete. Activated CCN are in the form of small solution droplets (typically with a radius around 1  $\mu\text{m}$ ) that further grow efficiently by the diffusion of water vapor [17].

As we can see from (figure 3.10) when supersaturation reach the highest level, droplets formation stops, and their average radii starts to grow.

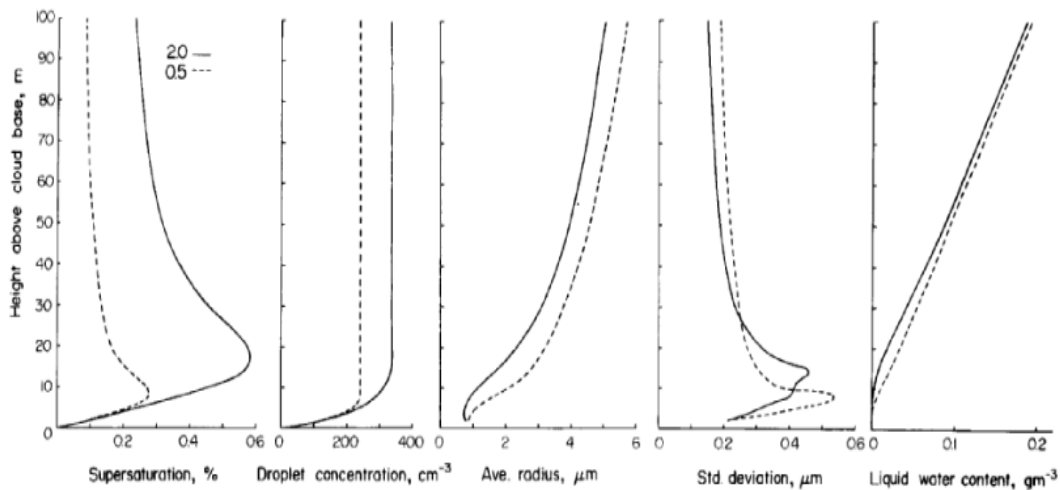


Figure 3.10: Early development of cloud properties in air ascending constant velocity of 0.5 m/s or 2 m/s.

### 3.4.2 Growth for diffusion/condensation of water vapour

During the diffusional growth, the rate at which the droplet radius increases is inversely proportional to the radius. This implies that a larger droplet grows (in radius) slower than a smaller one. This rate can be represented by the following simplified equation:

$$\frac{dr}{dt} \propto \frac{s}{r} \quad (\text{Equation 28})$$

Because small-sized droplets growth is faster than droplets with bigger radii, it is possible to argue that droplet size distribution (Figure 3.11) is narrower as mean droplet radius increases, supposing that all particles are exposed to the same supersaturation the big ones start to grow slowly, and the small ones achieve them [17].

However, it must be said, that generally, droplets are not all exposed to the same level of supersaturation. The outcome is that the resulting spectrum after the condensation phase is not as narrow as the analytical formulas would suggest (Figure 3.11), but tends thanks

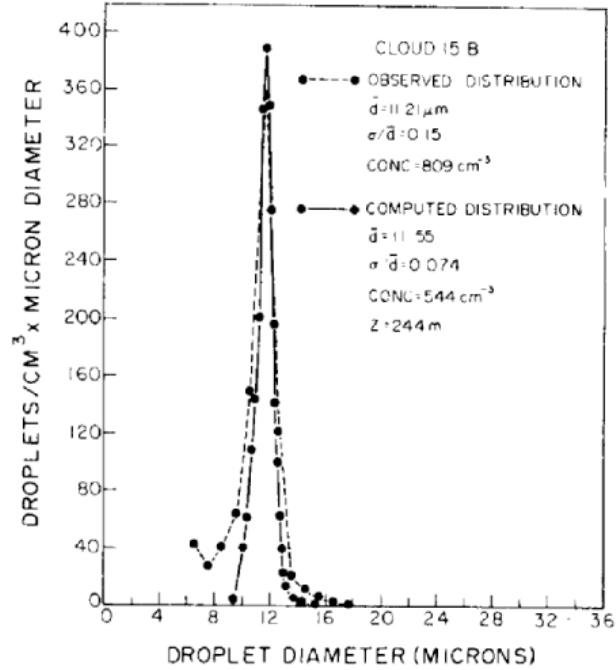


Figure 3.11: Comparison of computed and measured cloud droplet spectrum.

to the phenomena described above, to widen and, thanks to this widening, to favor the future process of coalescence.

Growth for diffusion and condensations occurs efficiently for droplets with radii smaller than  $15 - 20\mu\text{m}$ , beyond which it becomes negligible. Diffusional growth is a reversible process, as opposed to growth by collision-coalescence, which is defined as irreversible process [16], [20].

### 3.4.3 Growth for collision/coalescence

Gravitational collisions between cloud droplets, in which larger droplets grow by capturing smaller droplets by collision-coalescence, are effective when the droplet radius reaches approximately  $40 \mu\text{m}$ . Small droplets tends to follow streamlines of the air flowing around large ones, while larger droplets are hindered to do it because of their inertia, so they coalesce. This mean that, greater the difference between droplets size is, the larger collision rate result. In terms of droplets size distributions, this phenomenon means that the frequency of droplet collisions depends on the droplet spectrum width. Here is why a wider droplet spectrum favor the process of coalescence [20].

Another important aspect that influences the collision rate between particles within the cloud is altitude. Altitude is a factor that can increase the terminal velocity of the droplet (from 5% to 20%) and consequently enhance the collision efficiency: lower air pressure and density values would make the motion of the particles much freer, guaranteeing a higher speed. This means that in a cloud the major number of collisions and so the biggest droplets are located in the upper part (figure 3.12) [21], [17].

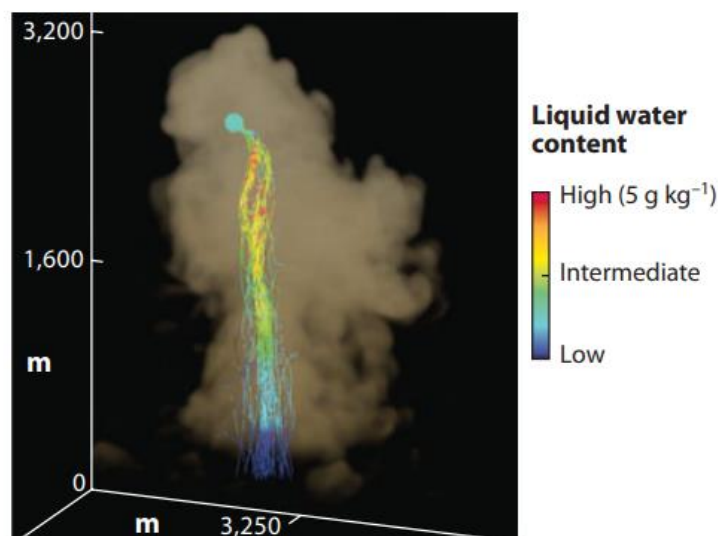


Figure 3.12: Simulation of a small cumulus, illustrating the idea of cloud-droplet growth through collision and coalescence processes.

In general, it is difficult to explain the rapid growth of cloud droplets in the size range  $15\text{--}40\ \mu\text{m}$  in radius for which neither the diffusional mechanism nor the gravitational collision-coalescence mechanism is effective. Because of the relatively low volume fraction of cloud droplets, collision-coalescence is primarily a binary local interaction of droplets. Each coalescence reduces the number of droplets by one count but conserves the total liquid mass. In (figure 3.13) we can see the difference in time rate terms about collision and diffusion growth of droplets [22].

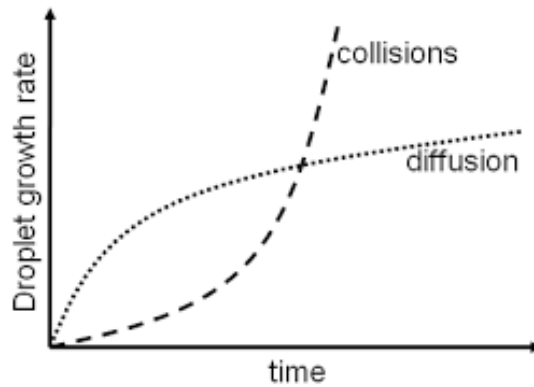


Figure 3.13: Droplet growth by diffusion and collision

### 3.5 Clouds Microphysics

Water concentration within a typical cloud (cumulus, stratocumulus) span from  $10 - 100$  droplets/cm<sup>3</sup> for small-sized droplets to  $1$  droplet/cm<sup>3</sup> for droplets with radii  $> 250\ \mu\text{m}$ . It is interesting to notice that, as mean radius increases, water concentration decreases, consequently spectrum peaks move to the right and downwards, broadening the spectrum shape [18].

It is necessary now to focus on the shape of the droplets spectrum as a function of the location within the cloud to investigate the microphysics of clouds a from what it is influenced.

Let us now imagine crossing a cumulus vertically, and to observe how the concentration of the droplets varies through the vertical and horizontal extension of the cloud. All this information were captured trough aircraft measurements.

- Vertical variability, as shown in (figure 3.14), [23] in cumulus clouds led us to observe that changes in concentration and size are not significant going up through the cloud.

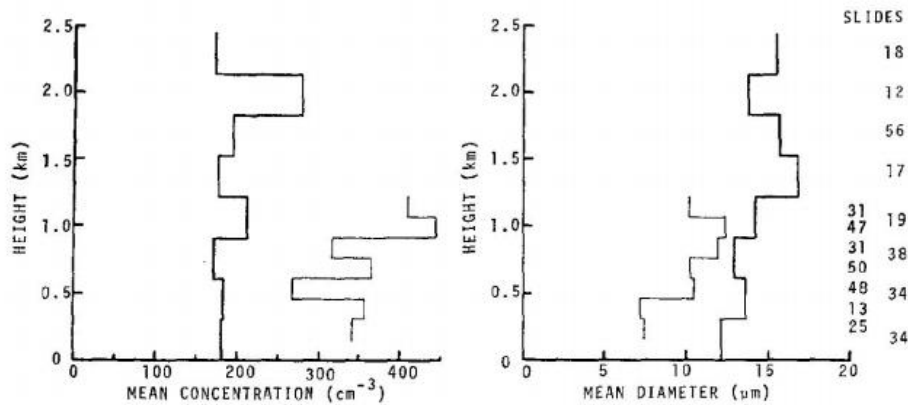


Figure 3.14: Mean droplets diameter and mean droplets concentration variation with height in cumulus clouds

However, it is present an increase in the range of large droplets that have low concentrations. Consequently, as shown in (figure 3.15), is visible a slight widening of the spectrum as the measurements were taken towards the cloud top, as well as an increase in frequency of bimodal distribution [23], [24].

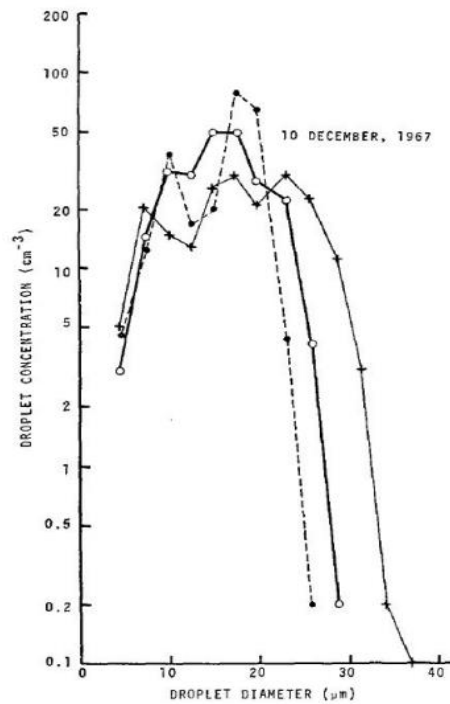


Figure 3.15: Three average spectra for different heights above the cloud base. •: 600m; ◦: 1100m; +: 1800m

- Horizontal variability: from the graphic below we can see wide regions of homogeneous droplets distribution (a) (figure 3.16) occasionally interrupted by micro-zones where droplet concentration drops near to zero (b). In correspondence of (c and d) we have the interfaces between cloud and still air, in fact the growth of number of drops is sudden [7], [25].

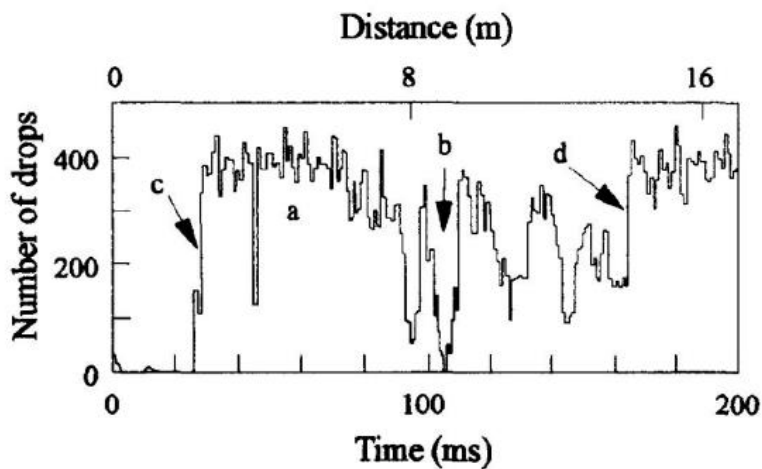


Figure 3.16: Droplet concentration measured at 1000 Hz during a flight through a small cumulus cloud.

### **3.5.1 Impact of Turbulence on Cloud Microphysics**

Clouds are intrinsically non-stationary, inhomogeneous, and are source of several fluctuating phenomena. Inside them we have a high level of turbulence and vorticity, a lot higher than around them, which mean that there is a strong interaction between different scales in both spatial and temporal systems. Obviously both fluid dynamics and microphysical processes play an important role in cloud evolution because they affect droplets growth, evaporation, precipitations and clouds radiative properties [26].

Droplets in a turbulent cloud are transported and dispersed by large-scale energy-containing turbulent eddies of the order of 100 m. At the same time, they alter the local environment through mass (condensation and evaporation), momentum (viscous drag), and energy (latent heat) transfer at the scale of individual droplets. These local transfers can lead to noncontact and contact interactions between droplets and together can modulate the background airflow. For example, the phase transformation between water vapor in the air and the liquid water in the droplets, taking place at the droplet scale, introduces bulk buoyancy effects that drive cloud-scale motions. The extreme density contrast between the droplet and the air implies a significant (at the microscale) droplet inertia and terminal velocity, making the droplet-turbulence interaction nonlocal and multiscale in nature [17].

### **3.5.2 Air Turbulence and Droplet Interactions**

Air turbulence in clouds is characterized by large flow Reynolds numbers, which implies that interactions take place over a large range of spatial scales (wide inertial subrange), [27] small energy dissipation rates (relative to many engineering flows) and moderate

velocity fluctuations. The dissipation rate  $\varepsilon$  is a key parameter and depends on the cloud type and age, with values around  $10^{-3} \text{ m}^2 \text{ s}^{-3}$  in stratocumuli,  $10^{-2} \text{ m}^2 \text{ s}^{-3}$  in cumuli, and  $10^{-1} \text{ m}^2 \text{ s}^{-3}$  or higher in cumulonimbus clouds [17].

Although cloud droplets are small ( $r < \eta$ ), their motion is tightly coupled with the air turbulence. This can be seen by comparing the droplet Stokes inertial response time:

$$\tau_p = 2\rho_p r^2 / (9\mu) \quad (\text{Equation 29})$$

and still-fluid terminal velocity:

$$v_p = \tau_p g \quad (\text{Equation 30})$$

to the Kolmogorov scales, where  $r$  is the droplet radius,  $\mu$  is the air viscosity,  $\rho_p$  is the water density, and  $g$  is the gravitational acceleration. For droplets with radii between  $10\mu\text{m} < a < 60\mu\text{m}$ , the Stokes number varies from 0.01 to 2, and the nondimensional settling parameter  $v_p/v_k$  varies from 1 to 40. Hence, the gravitational settling is almost always important, whereas the inertial effect is weak for small  $\varepsilon$  and significant for large  $\varepsilon$ . Both parameters increase rapidly with droplet size, which demonstrates the strong nonlinear nature of droplet-turbulence interactions [27].

### 3.5.3 Role of Turbulence in Droplets Motions

The motion of a small droplet in a turbulent flow field is governed by an equation with several complex terms (Maxey and Riley, 1983); however, under the conditions relevant for a cloud (i.e.,  $\beta \equiv \rho_d/\rho \gg 1$ , where  $\rho_d$  and  $\rho$  are the density of the droplet and air respectively) the equation can be simplified to:

$$\frac{\partial v_i}{\partial t} = \frac{(u_i - v_i)}{\tau_d} + g_i \quad (\text{Equation 31})$$

where  $v_i$ ,  $u_i$ , and  $g_i$  are the  $i$ -th components of the droplet velocity, the fluid velocity, and the gravitational acceleration vector, respectively;  $\tau_d \equiv \beta d^2 / (18\nu)$  is the *inertial droplet response time* which is defined as the characteristic time a particle takes to react to changes in flow;  $d$  is the droplet diameter; and  $\nu$  is the kinematic viscosity of air. The forces acting on the droplet are Stokes drag and gravity [27]. Droplet inertia is represented by *Stokes number* defined as:

$$St = \frac{\tau_d}{\tau_\eta} \quad (\text{Equation 32})$$

where  $\tau_\eta$  is the Kolmogorov timescale defined as  $\tau_\eta = (\nu/\varepsilon)^{1/2}$

If  $St \gg 1$ , particles react very slowly to flow changes, while with  $St \ll 1$  they follow the flow exactly. It is expected that preferential concentration results when  $St \approx 1$  [28].

The Stokes number can give information about the relative speed between particles and flow.

- $St \gg 1$  exist an important difference between droplets and flow, due to the inertia of the droplets.
- $St \approx 1$ , which mean that there will be a maximum relative velocity.
- $St \ll 1$  the relative velocity between droplets and flow is very low, in fact particles can follow the flow faithfully.

For a fluid with several particles dispersed, the trend will be very similar, but with much bigger relative velocity range, because motes of different sizes have different inertia and will follow the flow in a different way [29].

Another important parameter to study droplet motions is the *non-dimensional terminal velocity* defined as:

$$Sv = \frac{V_T}{v_\eta} = \frac{\tau_d g}{v_\eta} \quad (\text{Equation 33})$$

where  $V_T$  is the particle terminal velocity, while  $v_\eta$  is the Kolmogorov velocity scale.

$Sv$  significance is the importance of sedimentation in reducing the time of interaction between a droplet and an eddy whose size is equals the Kolmogorov length scale.

If  $Sv \gg 1$ , particles react very slowly with eddies, while with  $Sv \ll 1$ , the sedimentation can be neglected.

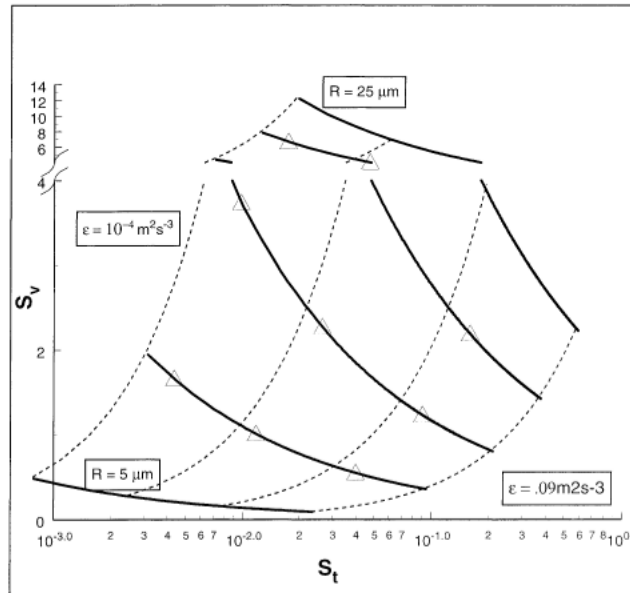


Figure 3.14: Velocity ratio-Stokes number ( $Sv$ - $St$ ) diagram for typical sizes of cloud droplets for an appropriate range of eddy dissipation rates. The dashed lines are for constant  $\epsilon$  while the solid lines are for constant radii.

In the limit  $St \ll 1$ , equation 29 can be simplified and we obtain the relation:

$$v_i \approx u_i + \tau_d g_i - \tau_d a_i \quad (\text{Equation 34})$$

where  $a_i$  term represents Lagrangian acceleration of the fluid at the particle location.

Looking at equation 34, it can be understood that droplets tend to move with surrounding air ( $u_i$ ), but with a relative motion resulting by:

- Gravitational settling.
- Inertial response of droplets to flow accelerations.

### 3.6 Entrainment and Large-Scale Mixing

Entrainment phenomenon is typical of the atmosphere, and it occurs whenever a turbulent stream, flows by a non-turbulent stream. It is an irreversible process by which a fluid particle approaches to the turbulent zone and acquires vorticity becoming part of it. The way in which entrainment occurs within a cloud could have important implications for the nature of the mixing process and the measure of spectrum widening that entrainment normally generates [31].

The entrainment–mixing process leads to formation of a cloud–environment interface zone (figure 3.15), consisting of the cloud dilution zone, where the liquid water content decreases as the distance from the cloud interior increases, and a humid shell with higher humidity in comparison with the dry environment.

The time evolution of the location and width of these zones is analysed by solving the diffusion–evaporation equation for the open region in the vicinity of the cloud–dry air interface [32].

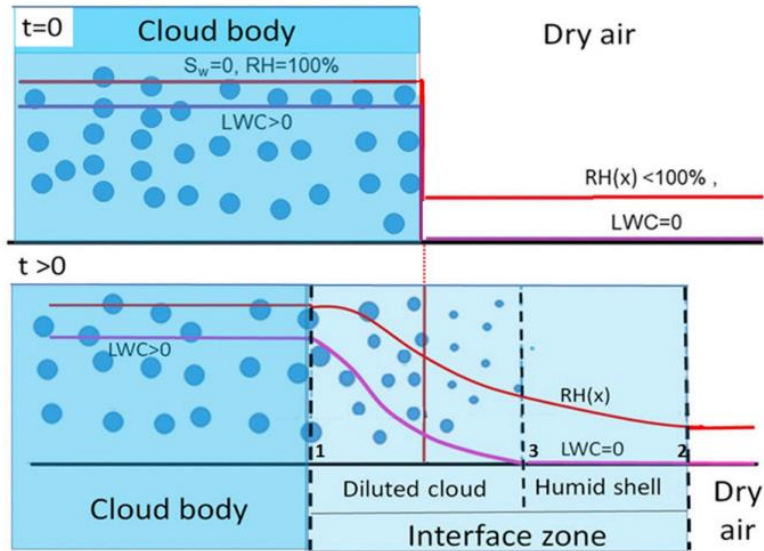


Figure 3.15: Conceptual scheme of zones in the vicinity of the cloud–dry air interface (top) at  $t=0$  and (bottom) for the developed interface zone. The initially sharp cloud–air interface is shown by red line in the top panel. Zone between vertical lines 1 and 3 is the dilution cloud zone. Zone between lines 3 and 2 is the humid shell.

### 3.6.1 Mechanism of Entrainment

The entrainment process of dry air inside the clouds takes place through 3 main steps.

- *Engulfment or nibbling* of dry air inside the cloud through the action of turbulence.
- Formation of mostly separate clean air and cloudy air filaments, phenomenon known as *stirring*.
- The filaments gradually become increasingly smaller, until they reach sizes in the order of  $\eta$ , a measure to which they become homogenized [31].

The term engulfment is often used to describe the phenomenon when it occurs due to large scale turbulent motions, while nibbling is used for small scale.

Simulations and laboratory experiments have shown that nibbling is a more often dominant process than engulfment, whereby it appears that molecular diffusion could be the dominant process. This is true if the level of instability resulting from turbulence does not increase significantly, because then nibbling would seem to become negligible.

The phenomenon of stirring is the direct consequence of the engulfment, dry and calm air that get in touch with turbulent air starts to accelerate and rotate due to the high level of vorticity and as consequence of this movement in starts to stretch into ever thinner filaments until this process end because an equilibrium condition is achieved (entrainment is completed) [33].

### **3.6.2 Consequences of Entrainment**

The first main consequence of entrainment process is the reduction of the liquid water content inside the clouds which influence the evolution of clouds droplets and the rain formation [32].

Entrainment in shallow cumuli has been shown to result in additional activation of entrained CCN: clear air supersaturated interacts with swirling structures associated with instability at the interface between the cloud and the environment. As a result, it penetrates inside the cloud, raising the level of supersaturation and thus promoting the activation of CCN [34]. Entrainment also involves a wide range of scales characterizing the turbulent transport of cloudy air upward within a cumulus cloud. As a result, droplets in the vicinity of a single point follow different trajectories through a turbulent cloud [17].

Considering a parcel with a certain supersaturation level which is subjected to mixing with a lower supersaturation level, there is a broadening of the spectrum. This type of mixing, in fact, slows the condensational growth of larger drops because the average supersaturation is lowered.

An important parameter that can give information about the way in which entrainment occurs is the *Damköhler number* that can be seen as rate between turbulence characteristic time and thermodynamic reaction time:

$$Da = \frac{\tau_r}{\tau_s} \quad (\text{Equation 35})$$

where  $\tau_r$  is the characteristic time of a turbulent vortex of radius  $r$ , while  $\tau_s$  is the characteristic time of a thermodynamic reaction related to the case under examination. In general, there are two different possibilities [7].

- If  $Da \gg 1$ , turbulent fluctuations are slow compared to thermodynamic reactions and can be in some cases neglected. As for the entrainment, in this case we speak of *inhomogeneous entrainment*, because the typical evaporation caused by the phenomenon cannot act uniformly, so some droplets will evaporate while others will remain unchanged. This implies a decrease in the number of droplets, but the average size remains unchanged, so there is not a significant difference in the spectrum [32], [7],
- When  $Da \ll 1$ , evaporation rate is the same for all the droplets, so they will all evaporate, but slightly, so that the number of droplets does not decrease, but the average diameter of all of them decreases. In this case of *homogeneous mixing*, for which we consider the entrainment instantaneous, the spectrum broads because there is a decrease of supersaturation [7], [31].

# Chapter 4

## The Radiosonde

Characterization of dynamics inside clouds remains a challenging task for weather forecasting and climate modeling as cloud properties depend on interdependent natural processes at micro and macro-scales. Turbulence plays an important role in particle dynamics inside clouds; however, turbulence mechanisms are not yet fully understood partly due to the difficulty of measuring clouds at the smallest scales. To address these knowledge gaps, an experimental method for measuring the influence of small-scale turbulence in cloud formation in situ and producing an in-field cloud Lagrangian dataset is being developed by means of innovative ultralight radioprobes [35].

Clouds are a natural complex feature of Earth and a key element in climate change and climate sensitivity, since their characteristics directly influence the global radiation budget, the global hydrological cycle (through precipitation), and the atmospheric dynamics. Clouds cover approximately two thirds of the globe at any time, and they are the principal source of uncertainty in future climate and weather projections. This is because clouds involve processes on a vast range of spatial and temporal scales, ranging from the order of few microns, where droplets nucleate and collide-coalesce, to the thousands of kilometres reachable by the larger storm systems. Clouds represent a substantial challenge for scientific understanding and modeling, since the available methods are not yet able to characterize the entire cloud system and related interactions across scales [36], [37].

Both the intense turbulence of the airflow hosting the clouds and the less intense turbulence that characterizes the environmental clear air surrounding them play an important role in cloud evolution and precipitation [20], [38].

Non-linear dynamical processes of vortex stretching, entrainment, and mixing greatly influence the nucleation of water droplets and associated evaporation–condensation and collision–coalescence [20].

Previous experiments with balloons filled with helium have been carried out [39], but the size of the balloon was too large to follow the trajectory of the current faithfully.

COMPLETE (Cloud MicroPhysics Turbulence Telemetry) [2], a Horizon 2020 project, was therefore launched by the need to create an in-cloud Lagrangian database and to develop an inter/multidisciplinary network capable of improving current knowledge about the complex multi-scale natural phenomena taking place within the clouds. One of the main tools with which COMPLETE intends to achieve its goal are insitu experiments, using an innovative light, floating, economical, biodegradable mini-radioprobe. To achieve its main the probe must attain 3 important aspects:

1. Floating on an isopycnic surface at a chosen altitude of about 1000m for a time spanning from the inner turbulence (scale of minutes) to the extension of cloud lifetime (few days), using a balloon filled with helium.
2. Acquiring atmospheric data (pressure, temperature, humidity) and location data through the employment of sensors.
3. Processing and transmitting the acquired data to a ground station using a mini antenna.

Atmospheric data will be captured through pressure, temperature and humidity sensor, in addition to movement sensors (accelerometer), which will capture data at regularly scheduled intervals [40]. Finally, the data will be interpreted, processed, saved and transmitted through a micro-antenna to a ground receiver [41].

## 4.1 Mini-Radioprobe Structure

These compact light-weighted devices with a maximum target weight of *30g* and diameter of *40cm* are designed to float at altitudes between *1–2 km* and be alive for approximately *1h-2h*. The radioprobes are capable of passively tracking small-scale turbulence fluctuations inside warm clouds and surrounding air since they can be considered as markers in a Lagrangian description of the airflow.

In order to enable them to float, the radioprobe electronics are housed inside 30 cm-diameter balloons made of biodegradable materials that are filled with an adequate mixture of helium gas and ambient air to reach a buoyancy force equal to the system weight [35].

The wireless sensor network (WSN) can be divided in three parts (figure 4.1):

- the green air balloon-wrapped radioprobe, which includes the solid-state sensors to measure the physical quantities of interest placed on the PCB, and which transmit the collected and pre-processed data to the ground.
- the base stations, which receive, store, and pass this information to the processing machine.

- the processing machine, which is used for database management, filtering, and visualization.

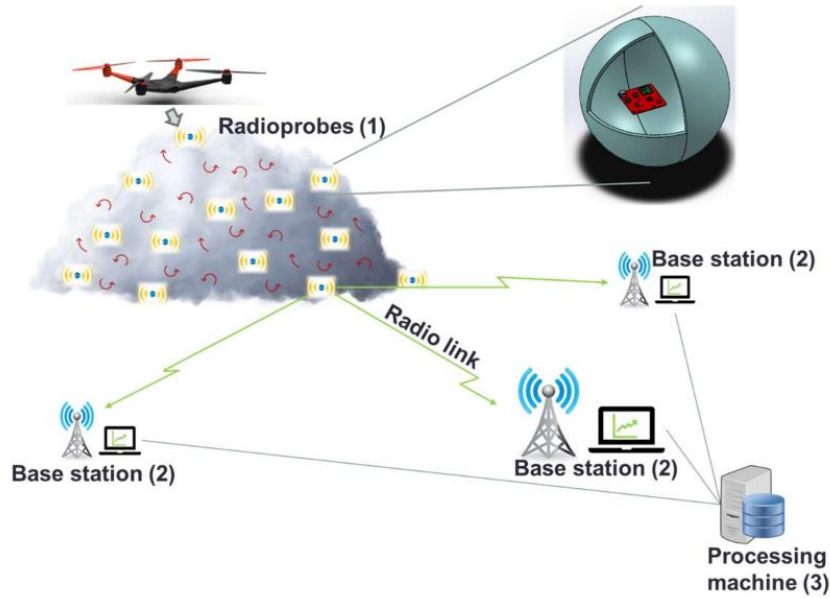


Figure 4.1: Scheme of the working principle and the radio-probe structure.

The printed circuit board (PCB) realization of the radioprobe is displayed in (figure 4.2). It is a  $50\text{mm} \times 50\text{mm}$  rectangular structure with a thickness of  $0.8\text{mm}$  and weight of  $7\text{g}$  (without the battery) [35].

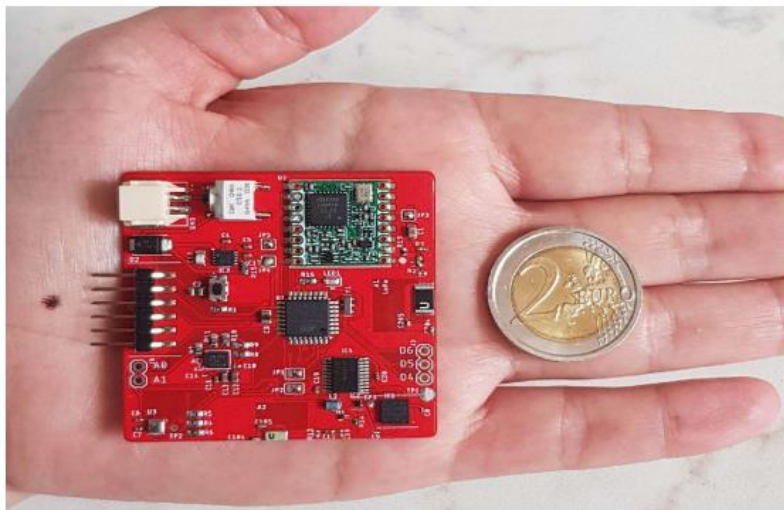


Figure 4.2: PCB implementation of the radioprobe. Size,  $50\text{ mm} \times 50\text{ mm}$ . Weight,  $7\text{ g}$

## 4.2 Characteristics of the Smart Material

The material used to produce the balloon has to satisfy different requirements for being able to perform its task correctly [42]:

- *Not too elastic*, because the probe is designed to maintain its volume constant. This is necessary also to keep the height of the probe almost constant; in fact, if it is too elastic, the helium inside the balloon would expand without problems.
- *Hydrophobic*, if not, water droplets inside clouds would tend to adhere at the surface with the consequence of a change in weight terms. This requirement can be satisfied using special coatings on the surface of the balloon but keeping in mind that it would imply an alteration of the weight.
- *Impermeable to helium*, it is clear that the more *He* would leak out of the balloon, the more altitude of the probe would decrease.
- *Cheap*, in fact because of the fragility of the probe, the light weight and that the use of GPS is not guaranteed, probes will not be recoverable. Several radiosondes will be produced, so the material must be cheap and easy to find.
- *Biodegradable*, as discuss above, at the end of its life, the balloon will be dispersed in the environment. This makes it necessary to be biodegradable.
- The material must guarantee a determined *inertia of temperature and relative humidity* between the inside and outside of the balloon: the sensors will be placed inside the balloon, so they may result insulated from atmospheric conditions and transmit incorrect data. To prevent this problem, the material must ensure that the temperature range  $\Delta T$  and relative humidity range  $\Delta RH$  are sufficiently low, with short transition times [35].

Several tests were carried out in laboratories to test the characteristics mentioned above on two different candidates: Latex, Mylar, PolyLactic Acid (PLA) and Mater-Bi.

Classic tensile strength tests have been carried out to evaluate the elastic capacity of the material. The samples were cut into the standard dog bone shape, 25 mm in length, 3.98 mm in width with the thickness being that of the material (30  $\mu\text{m}$ ), and the straining rate was set at 1 mm min<sup>-1</sup>.

To assess the hydrophobicity, the contact angle between a 5  $\mu\text{l}$  drop of water deposited on the surface of the film was obtained, which is the angle between the direction of the solid-liquid tension and the direction of the liquid-gas tension, tangent to the external surface of a drop, with the vertex at the three-phase liquid-solid-steam point (Figure 4.3). As the figure shows, the higher the contact angle value, the more hydrophobic the material can be considered.

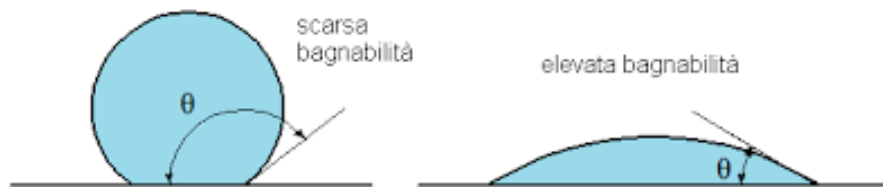


Figure 4.3: Contact angle of a drop on a solid material; a) Hydrophobic. b) Hydrophilic

To estimate helium permeability, balloons of the two materials were inflated with helium and placed on a scale, the velocity at which the weight of the balloons increase is directly connected with the extent of the helium loss.

Finally, to assess the difference in temperature and relative humidity between the inside and outside of the balloon, measurements were performed in the climatic chamber of INRIM, where values of  $\Delta T$  and  $\Delta RH$  can be chosen [42].

At the end the choice fell on Mater-bi, in fact, because of its characteristics, it turned out to be the most suitable material for our purpose. It is a bio-plastic, very cheap bio-degradable, and most important easy to find, in fact classic shopping bags are made of

| Material                                   | Mean contact angle [°] |
|--|------------------------|
| Latex                                      | 79                     |
| Mylar                                      | 95                     |
| Mater Bi                                   | 89                     |
| Mater Bi+carnauba wax                      | 125                    |
| Mater Bi+carnauba wax+Pine Resin           | 73                     |
| Mater Bi+carnauba wax+SiO <sub>2</sub> NPs | 140                    |
| PLA  | 83                     |
| PLA+carnauba wax                           | 126                    |
| PLA+carnauba wax+Pine Resin                | 81                     |
| PLA+carnauba wax+SiO <sub>2</sub> NPs      | 136                    |

Table 4.1: Contact angle for each material with different coatings

Mater-Bi. If we add the possibility of spreading coating on the material, its characteristics improves further as shown in the table below (Table 1). In particular, the coating that includes silicon nanoparticles significantly increases the contact angle [42].

### 4.3 Working Principle

The operating diagram of the mini radio-probe and ground system is shown in (Figure 4.4).

The left part of the diagram (marked in blue) is contained in the PCB (Printed Circuit Board) shown in (Figure 4.2), with dimensions of  $5 \times 5 \text{ cm}$  and weight of  $7 \text{ g}$ , placed inside the balloon.

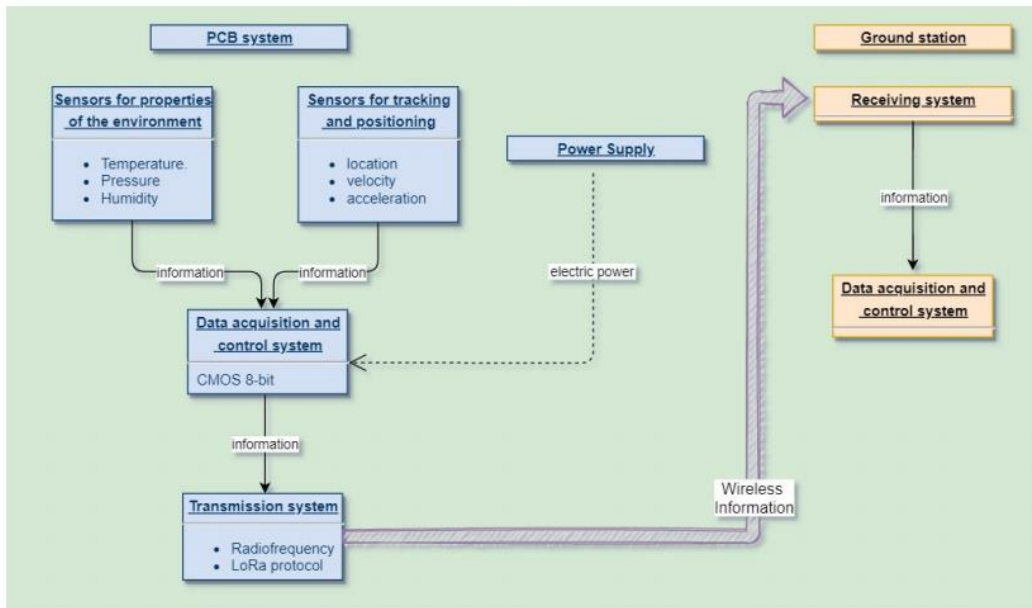


Figure 4.4: Flow chart of the radio-probe operating system.

The right part of the diagram (orange blocks) consists of the ground station, in which the data receiver system is present; data will be then further processed and analysed.

We now focus our attention on the components settled on the PCB :

- The first is a configurable all in one *set of sensors*: pressure, temperature, humidity and 3-axial accelerometer in the three directions (Figure 4.5) [43], [44].

## SENSORS



**BME280**  
 Humidity, temperature  
 and pressure  
 Operating voltage:  
 1.71 to 3.6 V  
 Operating range:  
 -40°C to 85°C  
 Dimension: 2.5 x 2.5 x 1 mm  
 Weight: approx.: <0.5 gram

**Diodes and transistors**  
**Other passive elements for signal conditioning**

Figure 4.5: PHT sensors Bosh BME280

1. *Temperature sensors* have a range from  $-40^{\circ}\text{C}$  to  $+85^{\circ}\text{C}$  with a resolution of  $0.01^{\circ}\text{C}$ .
2. *Humidity sensors* have a range from 0% to 100% with an absolute accuracy tolerance of  $\pm 3\%$  and a resolution of 0.008%.
3. *Pressure sensors* have a range from 300hPa to 1100hPa and a resolution of 0.18Pa
4. *Trajectory sensors* have an accuracy of about  $\pm 100\text{mm}$  and frequency rate smaller than 10Hz.

The sampling period for pressure, temperature and humidity is  $T_{sensors} = 2s$ , while the period for capturing trajectory is chosen to be  $T_{accelerometer} = 0.1s$ . To realize velocity and acceleration estimation, the chosen approach was radio signals combined with position estimation techniques to localize the target objects [43].

- To provide the energy necessary for the correct function of the radioprobe, one battery at *Lithium Metal Oxide* (LMO) and pulse current capacity of  $3.75A$  is used. The battery needs to be very small and lightweight; it is 23mm of height, 5.4mm of diameter, has a nominal voltage of  $4V$  and a nominal capacity of  $125mAh$ . The consumption is estimated of being almost  $50mAh$  without GPS and  $100mAh$  if we use GPS.

- The data-processing and control unit block is the computational module of the radioprobe. For this purpose, a *CPU* (CMOS 8-bit microcontroller ATmega 328) which is the brain of the control system (Figure 4.6) is used. It has 32 pins in a thin quad flat pack with compact dimensions and weight ( $9\text{mm} \times 9\text{mm} \times 1\text{mm}$  and only  $70\text{mg}$ ). In this unit, the data delivered by the sensors are interpreted, processed, saved, and sent through the transmission module to the ground using the small antenna placed on the PCB. To minimize the probe power consumption, the micro-controller maintains sensors in sleep mode until they must perform a measure. The same is for the transmission system.



*Figure 4.6: ATmega 328 microcontroller*

- The radio communication system is provided by a ceramic *omni-directional antenna* to transmit data to the receiver using radiofrequency signal. Information will be sent from the probe to a ground receiver, using the frequency bands around 350MHz or 169MHz. This permits to probe to be monitored at lower power during the entire flight through warm clouds because good propagation link and low attenuation are guaranteed.

The signal is required to be received up to 20km, and the receiver has a sensitivity about  $P_{receiver} = -130dBm$ . Each probe must transmit a power of at least  $P_{probe} = -30dB$  [45].

Due to the required criteria of the artificial floating probes, LoRa communication technology has been adopted. LoRa is a chirp spread spectrum (CSS) modulation technique, which encodes information in linearly increasing chirps [46].

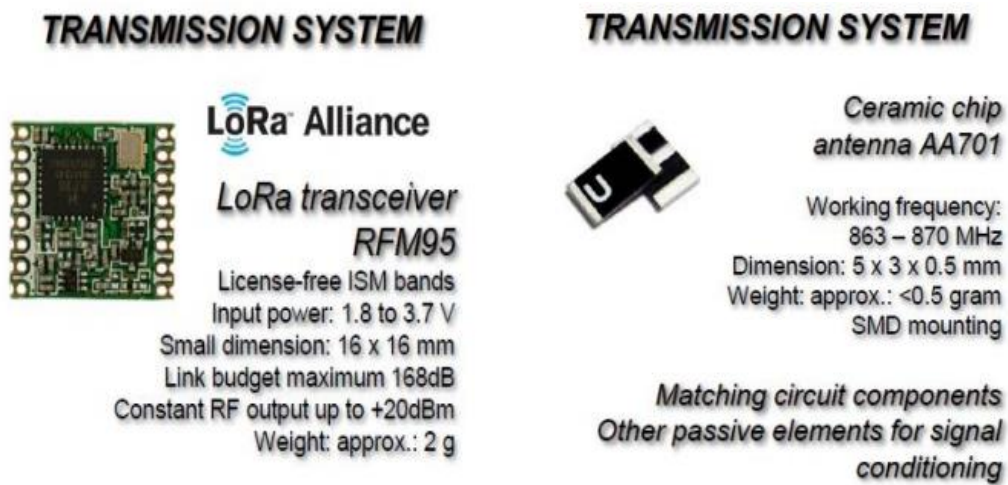


Figure 4.7: a) LoRa transceiver, b) ceramic chip antenna.

- The positioning and motion tracking is executed as a postprocessing task at the ground level and is obtained by sensor-fusion algorithms based on Kalman and orientation filters. The orientation filter is used to fuse data coming from an *inertial measurement unit* IMU, and the *Kalman filter* exploits the output of the orientation filter and fuses it with the data coming from a *Global Navigation Satellite System* (GNSS) receiver.

The IMU used for this block is the nine-axis inertial module device LSM9DS1 that combines a three-axis digital linear acceleration sensor, a three-axis digital angular rate sensor and a three-axis digital magnetic sensor, all in a

single package, the LGA package, of dimensions  $3.5\text{ mm} \times 3\text{ mm} \times 1.0\text{ mm}$ , requires a supply voltage in the range from 1.9 to 3.6 V. The GNSS receiver unit used in this block is a professional ultrasmall, super-low power system-in-package (SiP) ZOE-M8B module that offers a super-efficient (Super-E) mode option for improving the power consumption. It comes in an advanced soldered land grid array (S-LGA) package of dimensions  $4.5\text{ mm} \times 4.5\text{ mm} \times 1.0\text{ mm}$ , requires a supply voltage in the range from 1.71 to 1.89V [35].

# Chapter 5

## Mater-Bi Air Balloon

To develop a radioprobe capable of floating on an isopycnic level in the clouds, using a Lagrangian point of view to understand better turbulence inside clouds, to capture fluctuations, collect pressure, temperature and RH data, it is necessary to create a balloon that can provide stability and that can follow the stream faithfully without interfering with its development. It must follow passively the air flows without compromise turbulent structures, so it has to be very light, as much small in size as possible and biodegradable.

To ensure all these requirements the balloon must be as spherical as possible and the PCB with the battery, that affects considerably the gravity center of the radioprobe and so its stability, must be as much as possible in the centre of the balloon, in order to avoid undesirable oscillations that can compromise the measurements of the sensors.

A preventive estimation to determine the dimensions of the balloon must be done considering the air density at sea level and the helium density with which the balloon will be inflated. Obviously, we must know the exact weight of each component of the radioprobe to determine the total weight of the sonde that the balloon will have to carry up.

## 5.1 Preventive Estimations

First of all we need to understand which is the necessary helium volume to ensure the probe suspension is. The total weight of the structure must be balanced by the *hydrostatic thrust* (*H.T.*) that the helium volume can provide, hence:

$$H.T. = W_{tot} \quad (\text{Equation 36})$$

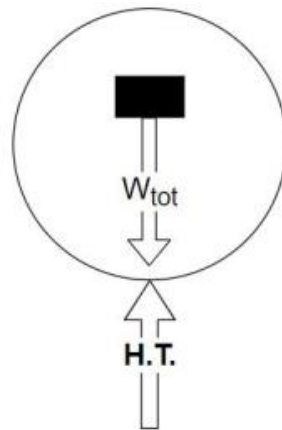


Figure 5.1: Equilibrium for hydrostatic thrust principle

Where overall weight is:

$$W_{tot} = M_{tot} * g \quad (\text{Equation 37})$$

The hydrostatic thrust generated by a lighter fluid ( $\rho_{he}$ ) than that in the external environment ( $\rho_{air}$ ) contained in a defined volume is:

$$H.T. = Vol * g(\rho_{air} - \rho_{he}) \quad (\text{Equation 38})$$

And we obtain:

$$Vol * g(\rho_{air} - \rho_{he}) = M_{tot} * g \quad (\text{Equation 39})$$

From which is easy to determine the helium volume necessary to keep the probe in suspension:

$$Vol = \frac{M_{tot}}{\rho_{air} - \rho_{he}} \quad (\text{Equation 40})$$

We can now introduce the molecular weights of helium and air and refer the equation to the air density:

$$Vol = \frac{M_{tot}}{\rho_{air} \left(1 - \frac{M_{he}}{M_{air}}\right)} \quad (\text{Equation 41})$$

where  $M_{He} = 4.003$  and  $M_{air} = 28.96$

It is important to keep in mind that air physical quantities are all altitude dependent, this means that we need to know how air characteristics vary with the increase of heights. In the troposphere (below 10 km) is quite easy to predict their values (figure 5.1):

| $Z$<br>[m] | $T$<br>[K] | $P$<br>$\times 10^4$<br>[Pa] | $\rho$<br>[kg/m <sup>3</sup> ] | $\mu$<br>$\times 10^{-5}$<br>[kg/ms] |
|------------|------------|------------------------------|--------------------------------|--------------------------------------|
| 0          | 288        | 10.0                         | 1.22                           | 1.79                                 |
| 500        | 285        | 9.5                          | 1.17                           | 1.78                                 |
| 750        | 283        | 9.3                          | 1.13                           | 1.77                                 |
| 1000       | 282        | 9.0                          | 1.11                           | 1.76                                 |
| 1250       | 280        | 8.7                          | 1.08                           | 1.75                                 |
| 1500       | 278        | 8.5                          | 1.06                           | 1.74                                 |
| 2000       | 275        | 7.9                          | 1.01                           | 1.73                                 |
| 3000       | 269        | 7.0                          | 0.90                           | 1.70                                 |

Figure 5.1: Relationship between altitude and air characteristics.

Now that we have the volume required for balloon, we can idealise it as perfectly spherical, this assumption simplifies the evaluation of the diameter:

$$d = 2 \left( \frac{3 Vol}{4 \pi} \right)^{1/3} \quad (Equation 42)$$

## 5.2 Balloon size

To determine the size of the balloon first we need to know the exact weight of the probe and all its components.

|                              | <b>Weights [g]</b> |
|------------------------------|--------------------|
| <b>PCB</b>                   | 7.5                |
| <b>Outer case</b>            | 10.5               |
| <b>Battery</b>               | 10                 |
| <b>Additional structures</b> | 2.5                |
| <b>Overall weights</b>       | 30.5               |

We can now proceed with the evaluation of the size of the balloon, firstly we assess the weight of the entire probe,

$$W_{tot} = M_{tot} * g = 0.0305kg * 9.81m/s^2 = 0.29921 N \quad (Equation 43)$$

which matches with the hydrostatic thrust:

$$H.T. = W_{tot} = 0.29921 N \quad (Equation 44)$$

The helium volume is, using the air density at sea level ( $\rho = 1.225kg/m^3$ ):

$$Vol = \frac{M_{tot}}{\rho_{air} \left( 1 - \frac{M_{He}}{M_{air}} \right)} = 0.0289 m^3 \quad (Equation 45)$$

Hence the diameter of the balloon required is:

$$d = 2 \left( \frac{3 \text{ Vol}}{4 \pi} \right)^{1/3} = 0.3907 \text{ m} \quad (\text{Equation 46})$$

in construction phase it will be approximate to *40cm* for convenience.

### 5.2.1 Balloon Assembly

The aim is to obtain a shape as spherical as possible without complicating the structure of the balloon. Mater-Bi is a very fragile material and small holes may form during the different processing stages. Therefore, it must be handled with care, especially during the welding phase.

For these reasons the balloon must be composed of as few parts as possible to limit the welding spots that are critical from the structural point of view, and which can cause deterioration of the material.

The instrumentation used to build and assemble the balloon are shown below:

- Bags of Mater-Bi with thickness of about  $30\mu\text{m}$ , available in any supermarket/hygiene shop.
- A surgical scalpel/cutter to cut the desired shape from the sheets of material.
- A ruler of about  $50\text{cm}$
- It is advisable to use a pen instead of an highlighter to draw the desired shape before cutting it.

- A *hand wheel sealer* with heated wheel connected to a handle (figure 5.2-5.2b).
- A Teflon tape to be applied on the heated wheel to prevent Mater-Bi from sticking to the wheel itself.
- A sheet of rubber/silicone to protect the work surface.
- A 99% of pure helium tank to inflate the balloons.



*Figure 5.2: Hand Wheel Sealer*



*Figure 5.2b: control knob to regulate the temperature of the heated wheel.*

### 5.3 Procedure

In order to obtain a balloon that respect the aimed characteristics in the following is shown the procedure step by step; the previous version of the balloon has been improved using an innovative method to create a spherical shape and a stronger structure:

1. Plug the hand wheel sealer into the socket and set the temperature at  $70^{\circ}\text{C}$  using the potentiometer (figure 5.2b). The heating systems requires some minutes to reach the optimal temperature. It is very important to operate at the correct temperature because Mater-Bi is very delicate and welding at more than  $70^{\circ}\text{C}$  can destroy the sheets of material. Anyway, before carrying out an important welding operation, it is advisable to perform a small test on a piece of waste material to evaluate the correct temperature of the sealer.
  
2. Build 4 sheets (shape A) and 1 (shape B) of Mater-Bi (figure 5.3).
  - Cut the seam at the bottom of the bag in order to create a bigger sheet.
  - Using a ruler and a pen, draw the desired shape (figure 5.3) on the sheet previously created with the correct dimensions; these are necessary to create a balloon with a diameter of  $43\text{cm}$ , in fact the  $3\text{cm}$  of surplus will be used in the welding phase.
  - Cut out the template using the cutter or the scalpel and trying to be as precise as possible.

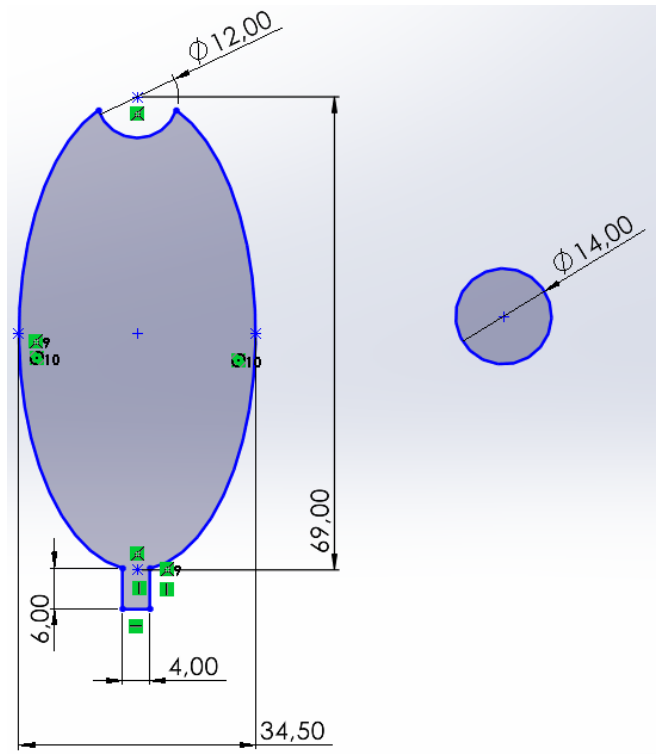


Figure 5.3: Shape A on the left and Shape B on the right with dimensions.

### 3. Construction of the pocket containing the PCB.

- From the waste cut a long strip of about  $3 \times 70 \text{ cm}$  and two squares of  $10 \times 10 \text{ cm}$ .
- Welds three sides out of four to create the pocket for the PCB.
- At  $20 \text{ cm}$  from one end of the strip, weld the pocket so that it remains in the center of the balloon once inflated.

4. Now proceed welding the four pieces (shape A) of the balloon together following their contour and being careful to leave one opening at the bottom to allow the helium inflation and another one to turn up the balloon and insert the PCB pocket, this operation will also help the weld to resist better when under pressure. In the

end add one piece of shape B at the top of the balloon to close it. Inspecting every weld can make the difference between success and failure.

5. Insert the PCB inside the pocket, connect the battery, close (by welding) the pocket and replace it inside the balloon then close the external opening. The balloon is now ready to be inflated.
6. Fill slowly the balloon with helium until it is inflated enough to push upwards all the structure. If it is bloated too much, we can have damage on the welds during its ascent.
7. Close the inlet using a wire or by welding it, during experiments that do not involve the loss of the balloon it is advisable to close it with a knot, so it is possible to reuse it.



*Figure 5.4: New version of the balloon, ready for the launch.*

# Chapter 6

## Data obtained from experiments

Several tests have been carried out to prove the instrumentation developed and to improve it. These kinds of tests are necessary when you have a prototype that needs to be improved and developed and sometimes it may be useful to conduct the same experiment in different conditions over a period, to verify the actual improvement of the instrumentation used and of the construction techniques.

### 6.1 Levaldigi Experiments

The experiments in this section were held at Levaldigi Airport, using the atmospheric balloon belonging to Envisens of the Vaisala probe, which considerably larger than ours (*1.30m of diameter*) and not biodegradable (latex) although deposable.

The COMPLETE PCB was placed under the balloon hanging through a thread like the sensor of Vaisala probe. Our aim is to compare the data coming from our probe and Vaisala probe, also thanks to ARPA Piemonte that gave us the possibility to analyse the data from their launch.

The results after the evaluation of the data were quite satisfactory which indicate the correct functioning of the probe, as shown in the figure below; our probe was able to transmit up over *8km* in height for a total distance of about *15km*, even more than what we expected.

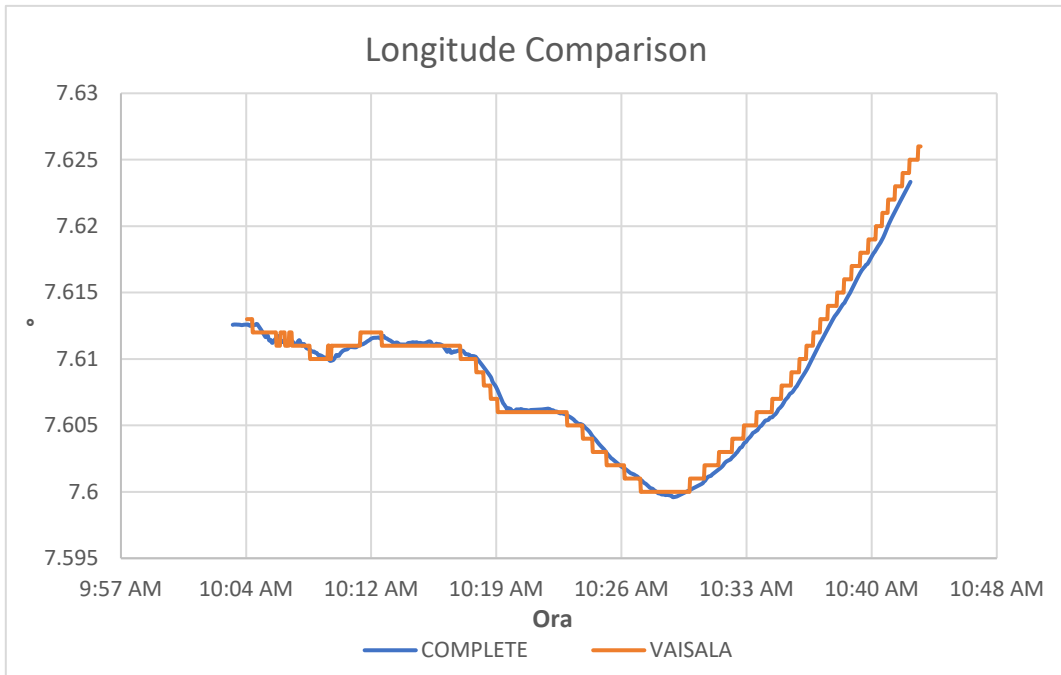


Figure 6.1: Radioprobe displacement comparison in Longitude.

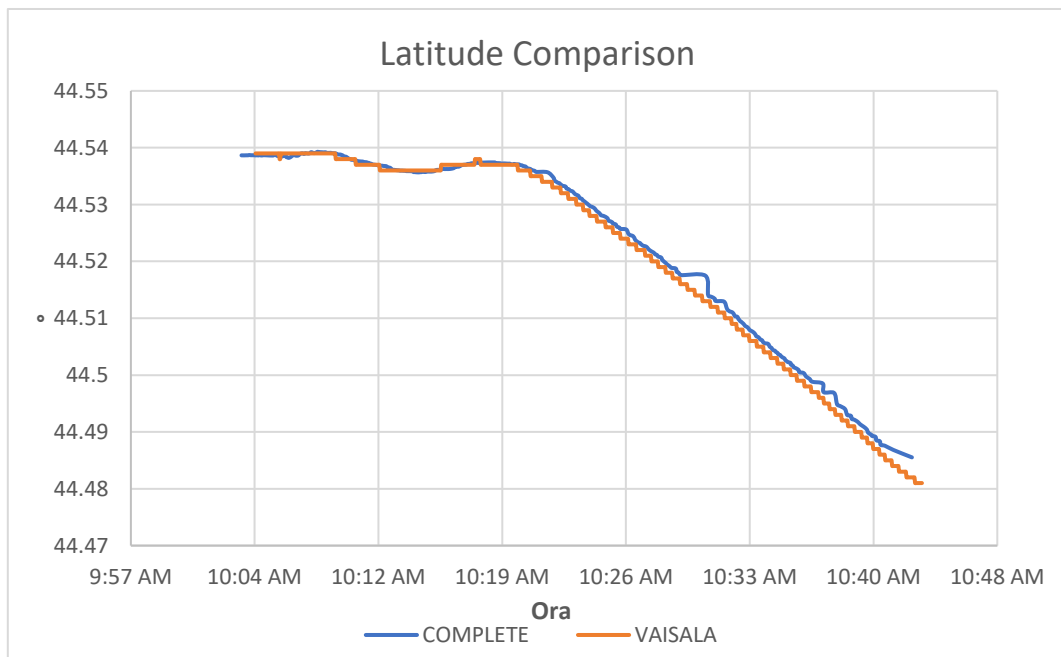


Figure 6.2: Radioprobe displacement comparison in Latitude.

We can see that GPS data were very accurate during the launch if compared with Vaisala ones. It took around 45min to lose the signal from our probe, after reaching almost 8.5km of height.

Also, on the pressure point of view we collected some interesting data as shown below:

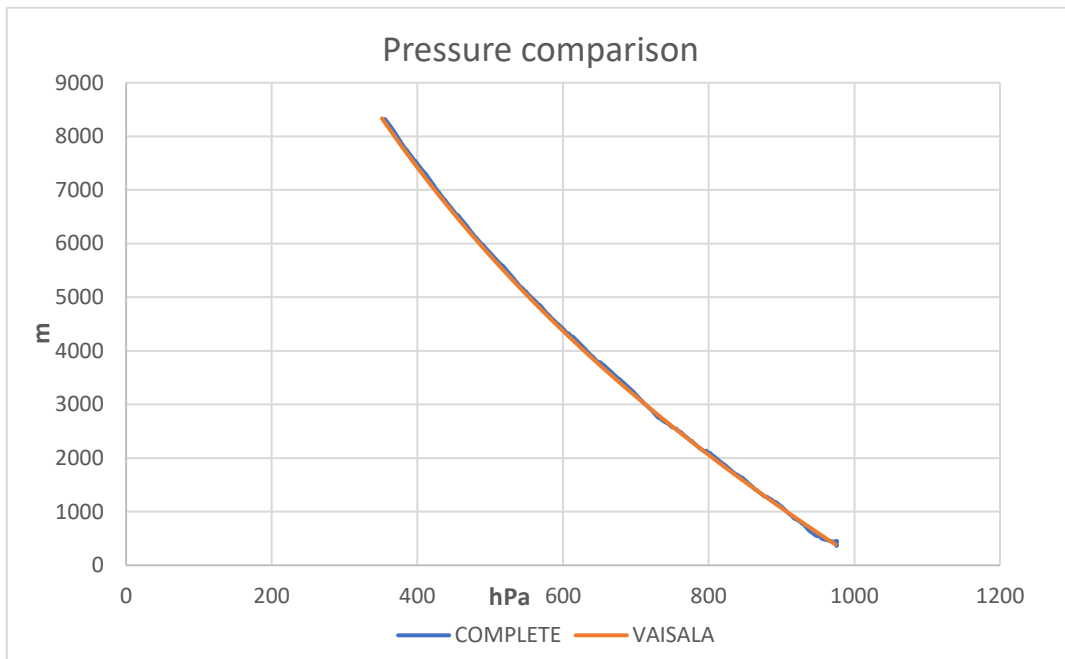


Figure 6.3: Pressure comparison related to height.

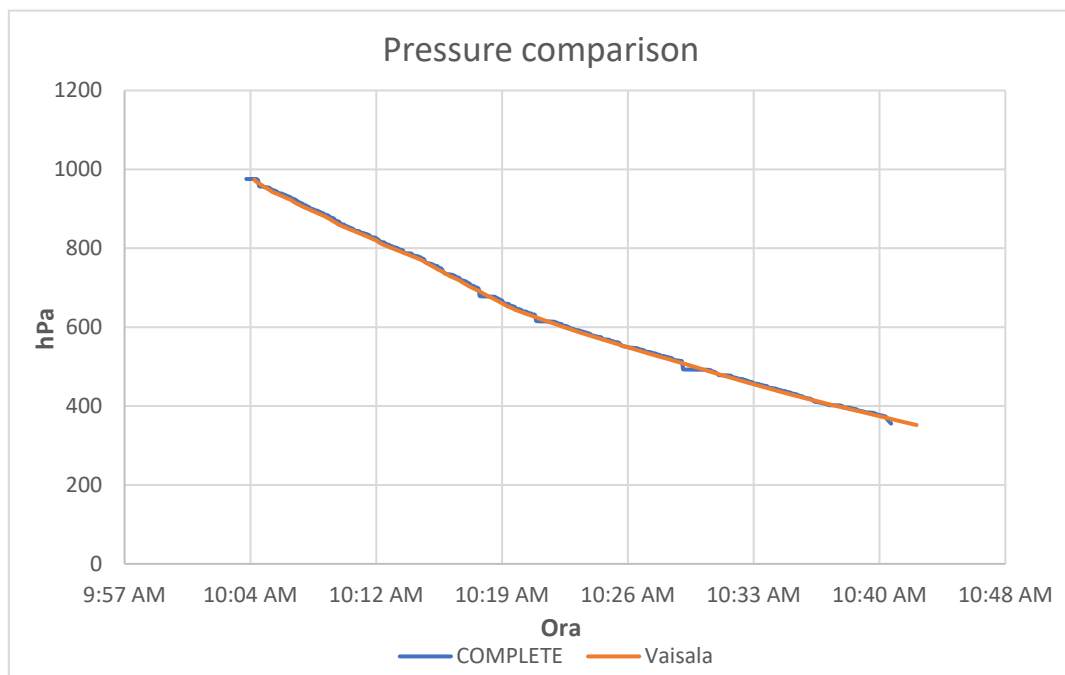


Figure 6.4: Pressure comparison related to daily time.

From both the graphics we can see that the pressure comparison is almost perfect between the two probes. This is a great result.

Let's now focus our attention on temperature trend:

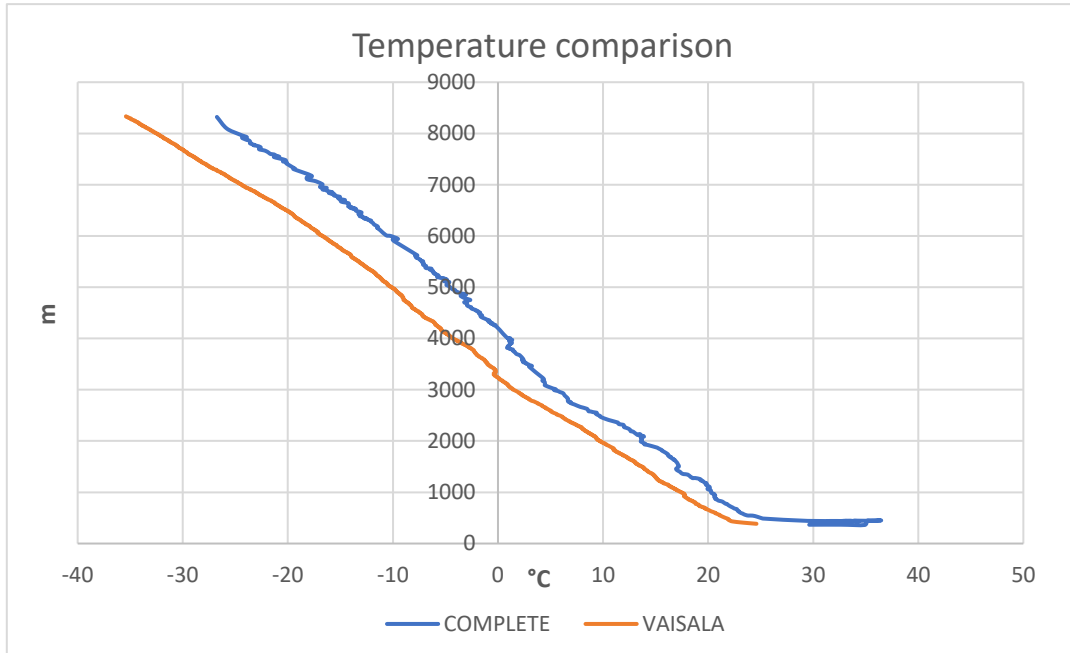


Figure 6.5: Temperature comparison related to height.

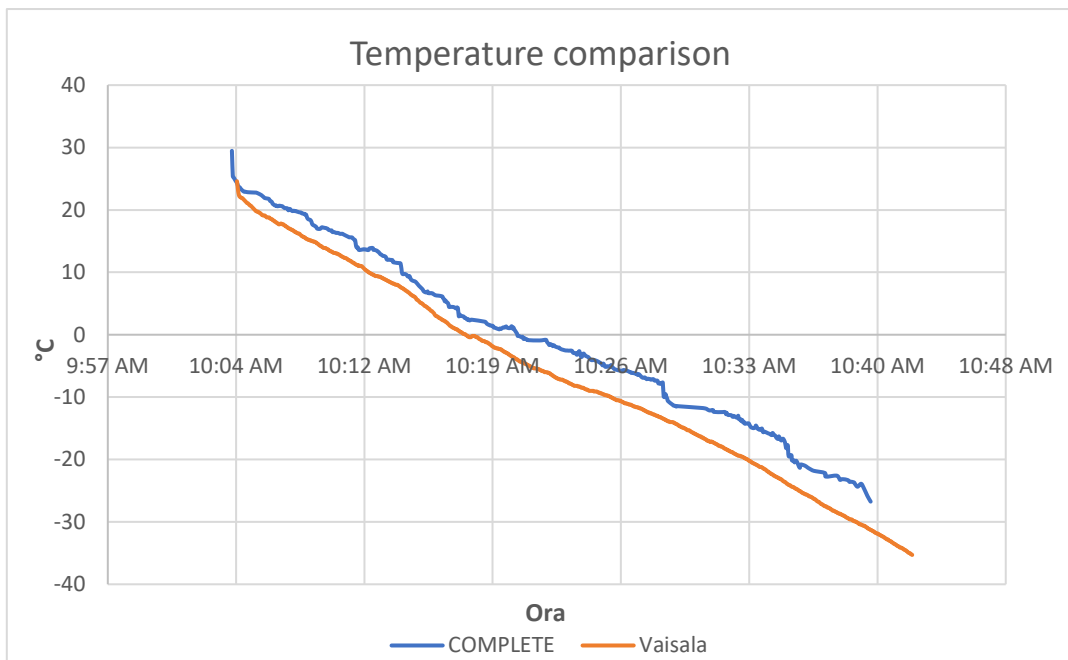


Figure 6.6: Temperature comparison related to daily time.

We can notice that the temperature comparison is not exactly superimposed although the qualitative trend is the same, in fact there is a constant offset between the two curves due

to a bias error. This probably happen because our temperature sensor is settled on the electrical circuit of the PCB which generates a slight overheating during the probe functioning owing to the passage of electric current from the battery.

The same problem occurs in Relative Humidity (*RH*) evaluation, as displayed in the graphs below.

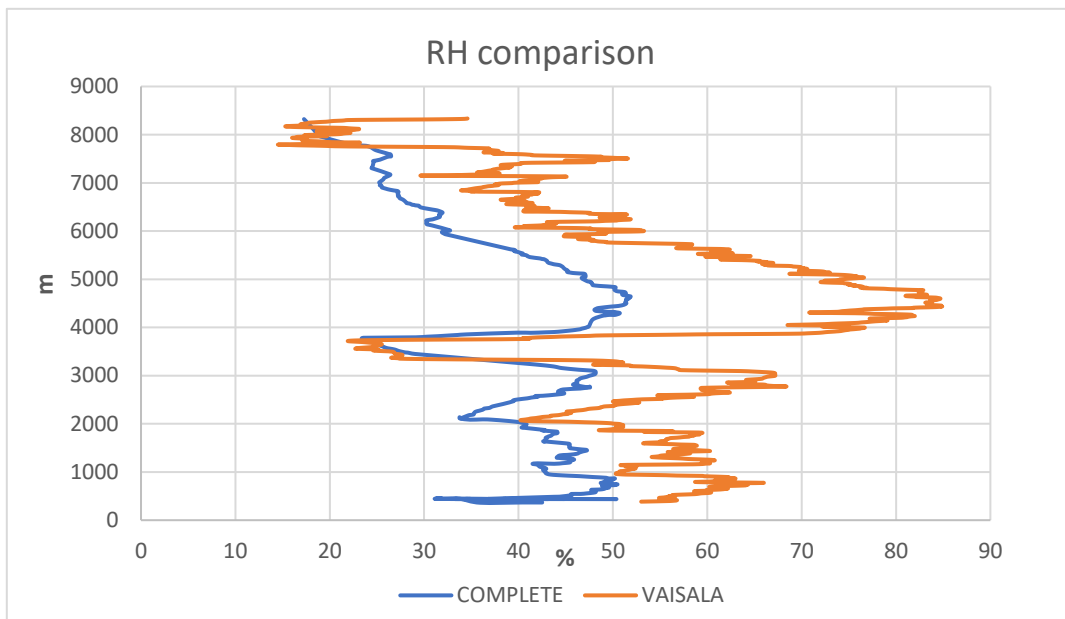


Figure 6.7: RH comparison related to height.

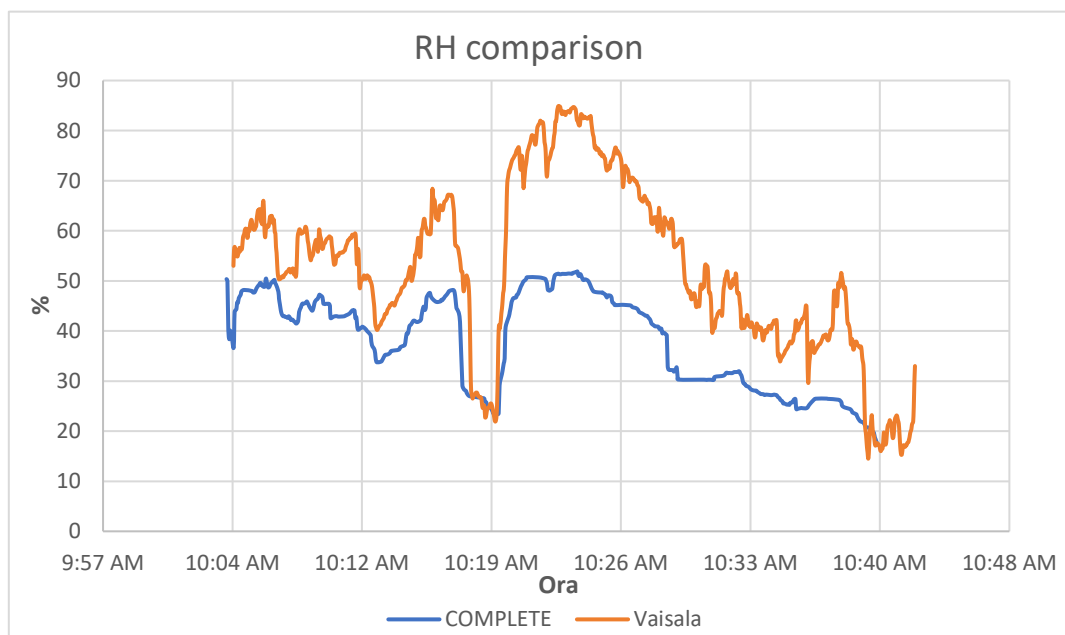


Figure 6.8: RH comparison related to daily time.

As we can see from the graphs, the qualitative trend of the two curves is the same but our probe seems to be affected by a delay in catching the fluctuations of the signal. This delay can be traced back to the bias error which also affects Temperature curve.

The last quantity we were able to assess is the wind speed, our probe in fact receives information about the wind speed coming from north and from east, at this point is very easy to evaluate the wind module and direction, using vector properties as shown below.

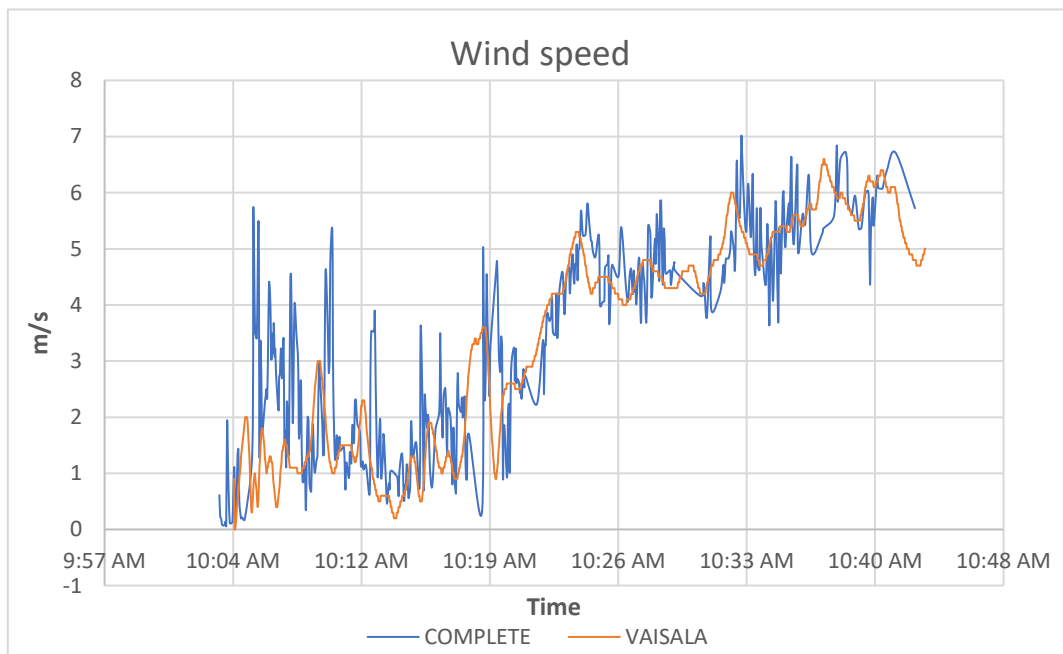


Figure 6.9: Wind speed module comparison between COMPLETE and Vaisala probe.

The qualitative trend is well represented on the graph although there are too many fluctuations on our data (*background noise*). This disturb may come from excessive oscillations of the PCB due to the thread through which it is hung at the air balloon that cause an irregular swinging of the probe.

The direction of the wind was evaluated as follow:

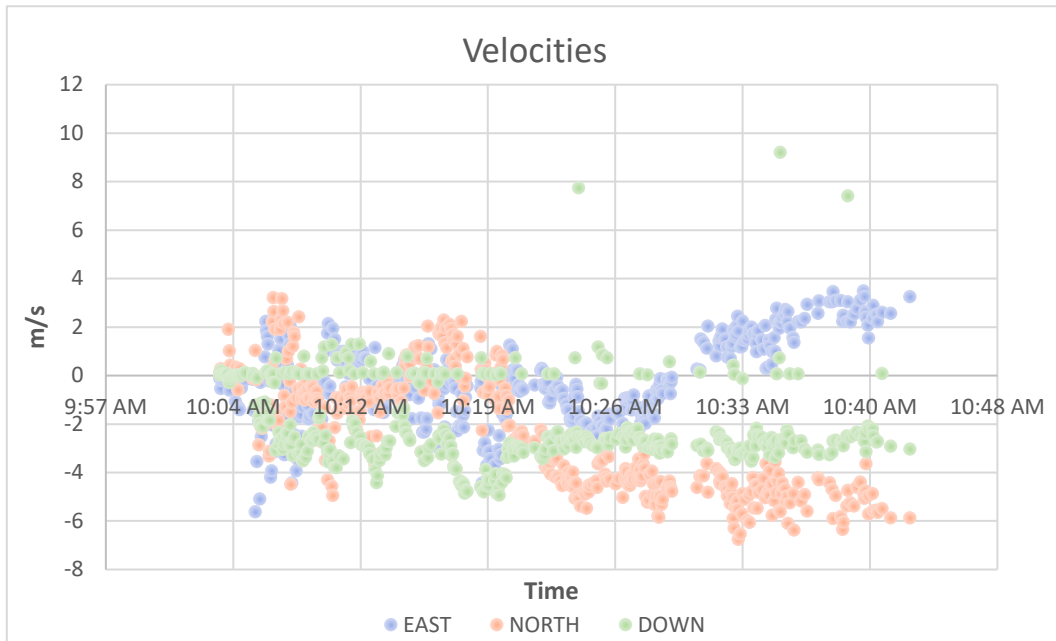


Figure 6.10: Wind direction data.

Whenever the value of the speed is negative, means that the wind was coming from the opposite cardinal point. (Example: -1 m/s from North, means 1 m/s from South).

## 6.2 INRiM Experiment

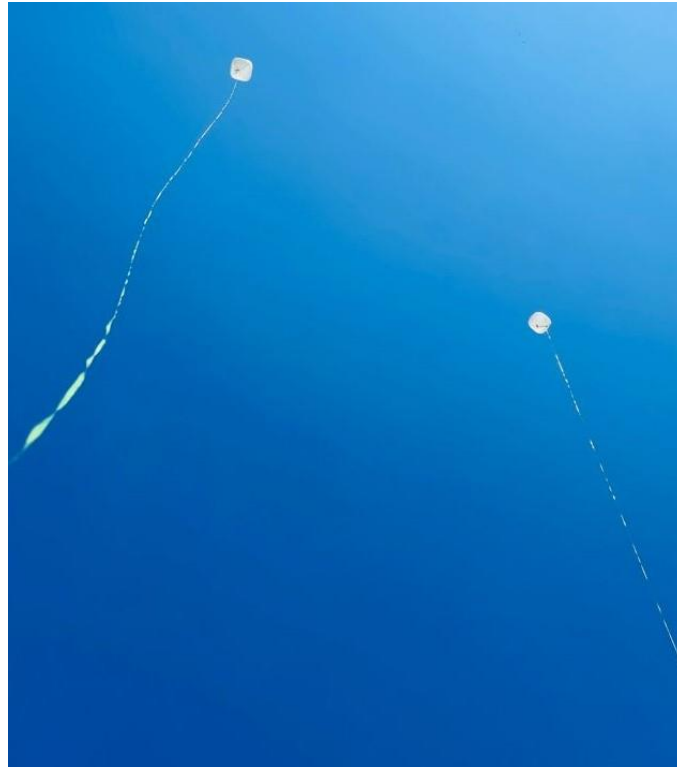
This experiment was held at INRiM (*Istituto Nazionale di Ricerca Metrologica*) in Turin close to the meteorological station in field. Our intention is to test the entire COMPLETE system: mini radioprobe, biodegradable balloon, transmission and data acquisition. It was the first in field test carried out with the new version of the balloon. On top of that we wanted to test the effect of balloon enclosure to pressure, humidity and temperature measurements. In order to reach our objective, we used two radiosondes simultaneously (figure 6.11):



Figure 6.11: The two PCB and batteries used for the experiment.

- Radiosonde 1 (RS1): radioprobe board (PCB) is inside the balloon, put in the pocket made by the same material as balloon (Mater-Bi) (id=24).
- Radiosonde 2 (RS2): radioprobe board (PCB) is outside the balloon, hangs on via thread and thread is attached to the ballon (id=20). After a while we decided to shorten the thread to avoid undesirable swinging of the PCB.
- To guarantee stability and precision in fluctuations reproduction a new version of balloons has been adopted which is more spherical than the previous and with the PCB placed as much as possible close to the gravity center.

The balloon was tied to a cord so that it could not be dispersed. This has made it possible to carry out the tests on data transmission/acquisition and the effectiveness of the balloon structure, but without wasting components that can be used for other tests in the future.



*Figure 6.12: RS1 and RS2 floating during the test*

After the setup of the two sondes, we carried out some measurements near to the meteorological station: low altitude, radiosondes are close to each other, few fluctuations. Then we moved in the stadium, receiver station is still near to meteorological station. Different altitudes (up to 10 meters), some fluctuations. During this phase of the experiment, we had some problems with the data transmission, especially from RS2, which caused a loss of information.

Despite these problems, our probes were able to transmit for more than 3 hours, more than what we expected.

This is what we obtained from our measurements:

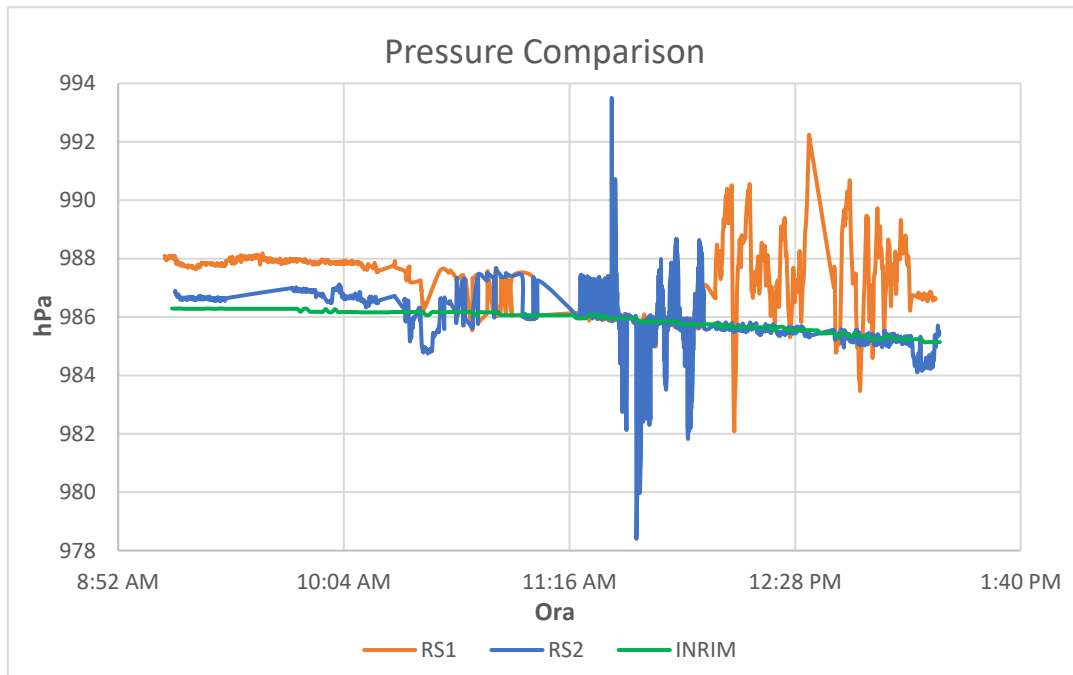


Figure 6.13: Pressure comparison between RS1, RS2 and INRiM station.

From the comparison we can see that the qualitative trend is represented quite good, in particular for RS2, but we have many fluctuations which can be traced back to the various displacement that our probes have suffered.

In addition, because of the thread, the two sondes were not able to float freely in the wind and sometimes they got stuck on the floor or in some obstacle. Anyway, we can see that RS2, with the PCB outside the balloon, has collected more accurate data than RS1. This is very important for the future development of the probe because it means that the pocket for the PCB is not strictly necessary and the probe can float outside the balloon.

The same happens for temperature data, as we can see from the diagram (figure 6.14), RS2 follow quite well the general trend but we have a lot of disturbs and oscillations.

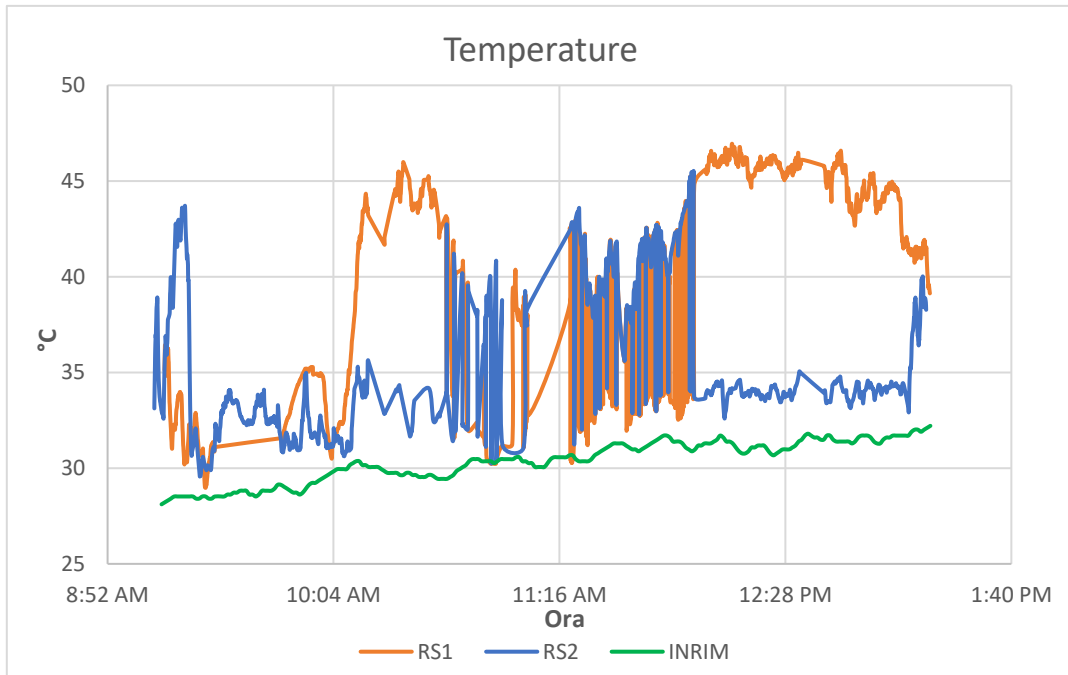


Figure 6.13: Temperature comparison between RS1, RS2 and INRiM station.

We can see that the bias error described previously is much less intense if the PCB is placed outside the balloon, in fact the overheating is reduced.

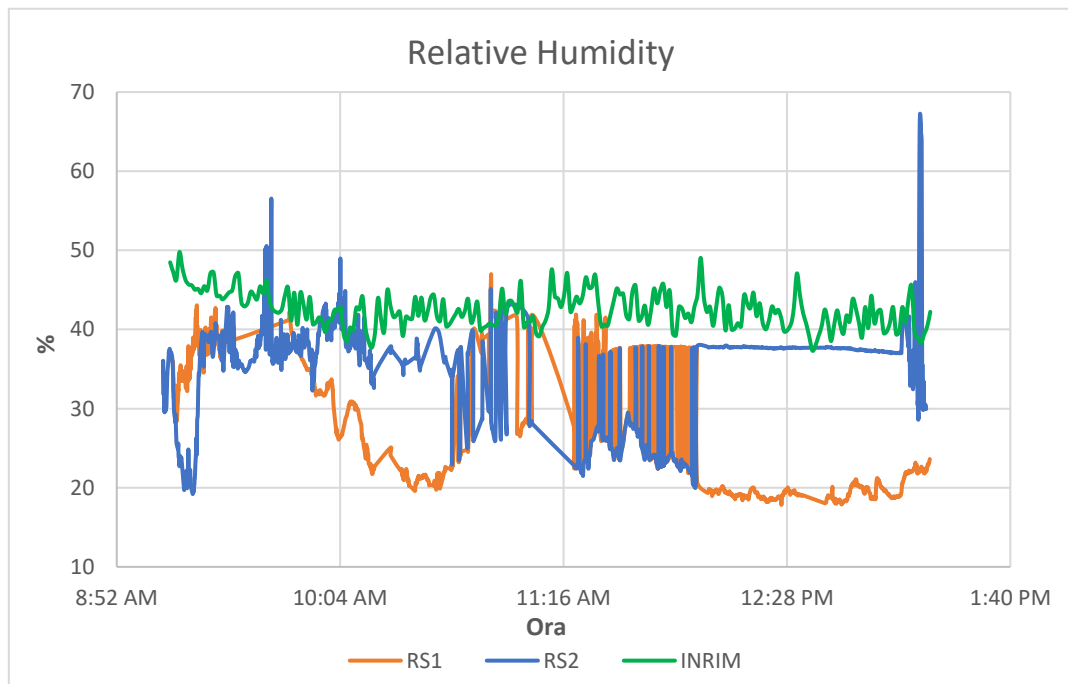


Figure 6.14: RH comparison between RS1, RS2 and INRiM station.

The same happen with RH diagram, we have unwanted fluctuations especially for RS1 but the bias error is reduced for RS2.

### 6.3 INRiM Experiment #2

This experiment was held at INRiM in Turin like the previous one next to the meteorological station in field. The main difference between the two experiments is that for this one we used 5 radioprobes (RS1, RS2, RS3, RS4, RS5) working all together at the same time. To avoid unwanted data loss, we prepared two different receivers, each one receives the information coming from every radiosonde in real time during their flight, so if one receiver lost the signal, we are still able to collect data thanks to the other one. In the picture below are shown the five PCB used for the launch (figure 6.15).

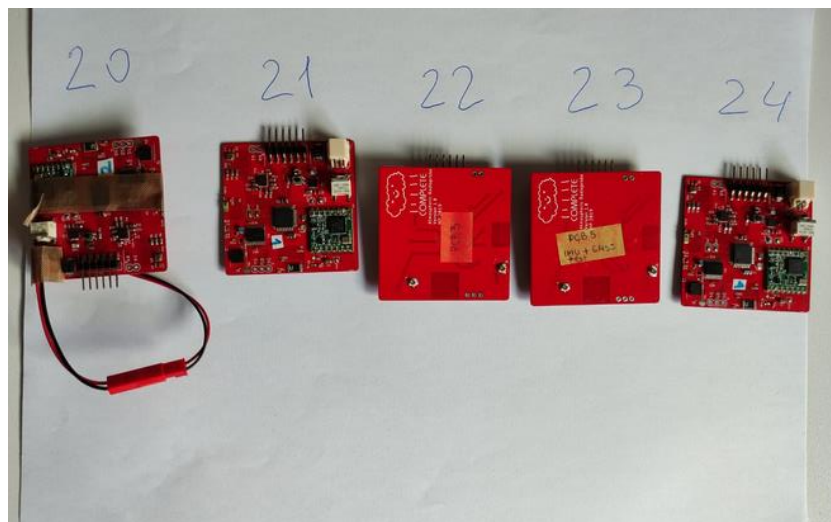


Figure 6.15: A picture of the 5 PCB used in this experiment with respectively Id.

The aim for this experiment is a little bit different from the previous one in which we only wanted to check the correct functioning of the probe as a whole, in fact our goal is to evaluate the relative dispersion of the radiosondes due to the turbulence flow.

We collected data of the relative positioning from the probe during the flight and then we analysed how they evolved. To achieve our goal, we used a MATLAB code, quite similar to that one used in the *paragraph 2.2* about *Turbulent Dispersion* and based on Richardson's experiment.

To verify the correct operation of the GPS sensor settled on the PCB we decided to shoot with a professional video camera the flight of two out of five balloons. In this way we were able to acquire the correct distances of the sondes from the single frame of the video by counting the image pixels that separates the two radioprobes.

At the beginning we ran into some problems with the balloons inflation, this setback made us waste a couple of hours but after that everything went as planned. We were able to launch five balloons simultaneously and collect information from all of them in real time using the two receivers.

To be sure of always shooting with the camera the same balloons and to not confuse them with each other we used a coloured spray can (black and red) to distinguish them.



Figure 6.16: Picture of the five radiosondes during the launch with red and black ones.

Information received from the two ground stations used, GS1 and GS2, were very accurate; for each sonde we were able to determine its trajectory by information of longitude and latitude.

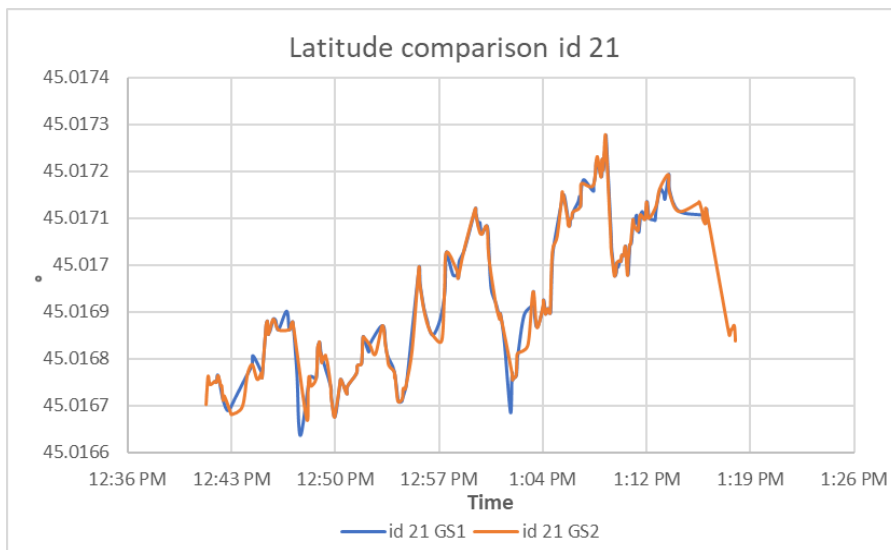
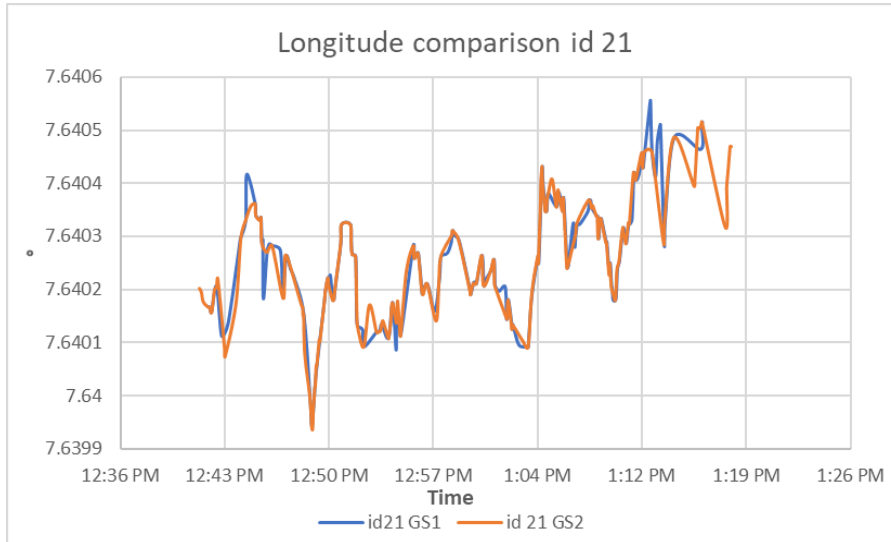


Figure 6.17: Longitude and Latitude comparison between GS1 and GS2 data for RS1.

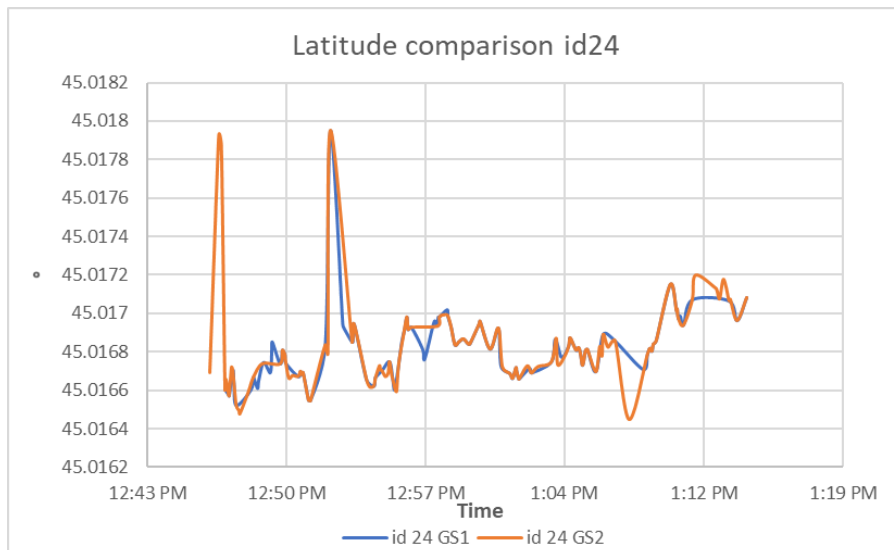
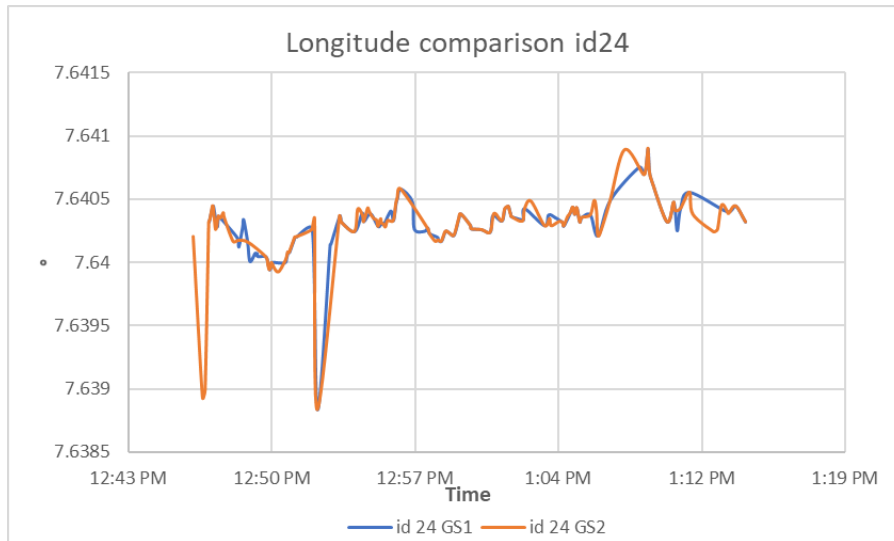


Figure 6.18: Longitude and Latitude comparison between GS1 and GS2 data for RS4.

As we can see the data from GS1 and GS2 are absolutely in agreement. This indicates the quality of the data acquisition system. We decided to use two different receivers to avoid and limit the phenomenon of data loss.

The five probes worked properly for more than an hour during which we were to obtain the information to trace the path taken by each of them. Using longitude, latitude, and altitude data it was possible to determine the trajectory and represent it in a 3-D

diagram. This is the first step to evaluate then the relative positioning during the flight of each radiosonde due to turbulent dispersion.

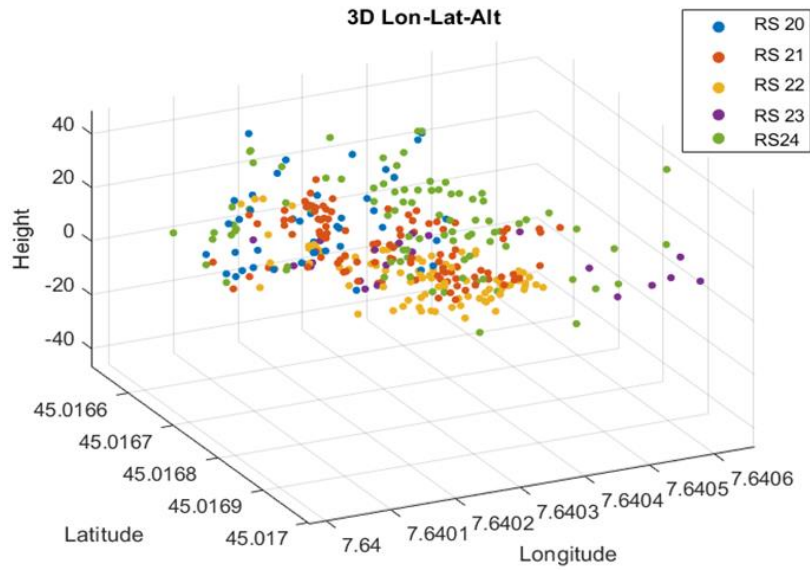


Figure 6.19: 3-D diagram which represent the shift in longitude, latitude, and altitude for each radiosonde.

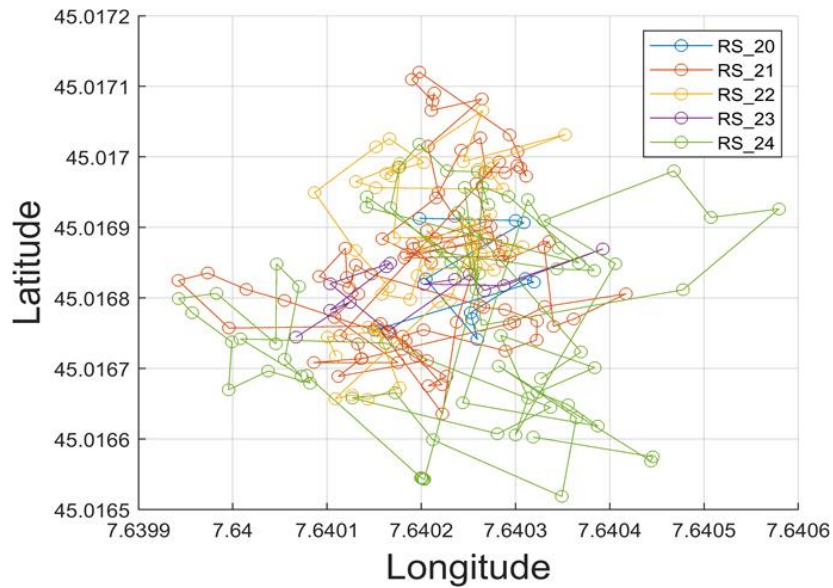


Figure 6.20: longitude and latitude trajectory for each radiosonde.

# Chapter 7

## Conclusions and Future Developments

This thesis initially illustrated the issues concerning the partial knowledge that scientific community has regarding clouds and their evolution, the growth of droplets and the consequent development of rain.

Turbulent dispersion within the clouds considerably complicates the understanding of the phenomena taking place inside the clouds, but it is also demonstrated how turbulent phenomena considerably modify various phases of the development of droplets and how important are for the clouds behaviour. It was subsequently explained how the lack of information is partly due to a scarcity of data from in-situ measurement, especially from Lagrangian point of view.

The Horizon2020 Innovative Training Network Cloud-MicroPhysics-Turbulence-Telemetry (MSCA-ITN-COMPLETE) project was illustrated, which aims is to develop a small radiosonde capable of floating in the clouds and transmitting Lagrangian-type information in real time. The operating principle of the probe was shown, and every electronic component was described in detail. Several tests were performed for the choice of the best material for our purpose with which the balloons are made. Several calculation and analysis were made to estimate the right dimensions of the balloons necessary for the correct suspension of the probe in mid-air; the weight of every single component of the PCB was essential to assess the needed hydrostatic thrust, and many tests were carried out in the Laboratory to design and develop the best shape of the balloon without complicating too much the structure given the fragility of the Mater-Bi.

The experiment we held brought an essential contribution to the development of the probe; the first one at Levaldigi showed excellent results (compared with Vaisala probe) ensuring the correct functioning of the electronic part of the radiosonde. The probe worked for more than 2 hours, and the signal was received from more than  $8.5km$  away. The data referred to pressure, temperature, relative humidity, and wind speed transmitted to the ground station were in perfect agreement with those received from the Vaisala probe of ARPA.

The second test, held at INRiM, was the first in situ experiment to verify the probe as a whole, a new version of the balloon was brought for the launch, lighter and more spherical, and for the first time we used two radiosondes at the same time. We had some problems with the reception of the information probably due to the presence of obstacles and the use of a less powerful receiver anyway we were able to collect a great amount of data, in fact the batteries lasted for more than three hours. The results from the analysis were not completely satisfying but gave us the opportunity to better understand the correct functioning of the PCB and its physical positioning in relationship with the balloon.

The last we made, just few days ago, required for sure the biggest effort from everyone. We wanted to test five radiosondes all together, it was very challenging. Our goal was to study and obtain a qualitative conception about the dispersion of the probes due to turbulence diffusion, by analysing the relative position between the sondes during their flight. To achieve our objective, we used two different receivers, and we shot using a professional video camera, the balloons while fluctuating in mid-air. For the numerical analysis we created a MATLAB code which receive the 3-D coordinates of the sondes at different instances as input and elaborates the number of nearby balloons per length as output. The results were quite satisfactory, the information acquired were very accurate

and we were able to trace the path taken by each probe. This is the first step to develop in the future an algorithm to evaluate the relative positioning between every single rarioprobe with the other.

## Ringraziamenti

Colgo innanzitutto l'occasione per ringraziare la mia relatrice, la Professoressa Daniela Tordella per l'aiuto e il sostegno profuso nei miei confronti durante questi mesi, sempre disponibile e paziente. Un altro ringraziamento va al dottor Shahbozbek Abdunabiev per essere stato una figura di riferimento in questo percorso e a Mina Golshan per avermi aiutato ogni qualvolta ne avessi bisogno.

Grazie alla mia famiglia per il supporto in primis morale ma anche economico che nell'arco di questo mio percorso non è mai mancato: grazie a mia mamma per ogni suo consiglio e parola dolce anche a distanza, a mio papà per essere una guida amorevole ed esempio da seguire, a mia sorella per essere la mia più grande tifosa, sempre al mio fianco, e a rudi il mio fratellino peloso.

Un grande grazie va a Clara per amarmi, aiutarmi e sostenermi sempre, ogni giorno mi permette di essere un migliore me.

Un grazie agli amici di una vita, Fede, Nirva, Lollo, Richi che ci sono sempre stati anche se le strade intraprese ci hanno portato distanti; un enorme grazie va a Greta per avermi sempre sostenuto malgrado tutto, molto di ciò che ho raggiunto e che oggi sono lo devo a lei. Gli amici del Liceo, Botti e Nico con cui ho condiviso tanto e ancora oggi ci sono sempre.

Un grazie al Race Off Team, i miei compagni di scannate in moto, dei pazzi di primo ordine ma che, come spesso accade, sanno regalare veri momenti di spensieratezza e amicizia.

Ultima ma non per importanza ringrazio la mia “seconda” famiglia qui a Torino, tutti i miei compagni di avventure con i quali ho costruito un legame indissolubile, mi avete accompagnato ogni giorno in questo percorso e non avrei potuto chiedere di meglio. Un grazie particolare va agli Aerospeciali, Gio, Cesa e Dome con i quali ho condiviso le gioie e i dolori della vita universitaria, ai miei coinquilini acquisiti Parmi e Kikka, alla Beddazza, al Compà e a tutti quelli che non nomino ma che so quanto siano stati importanti in questo percorso.

# References

- [1] J. C. R. Hunt – “Lewis Fry Richardson and his Contribution to Mathematics, Meteorology and Models of Conflict” Annual Reviews Fluid Mechanics Cambridge 1998
- [2] “Horizon 2020; Call: H2020-MSCA-ITN-2015-ETN - Proposal Submission Forms”, Research Executive Agency, vol. 675675, 2015.
- [3] Geoffrey K. Vallis – “Essential of Atmospheric and Oceanic Dynamics” Cambridge University 2019
- [4] G. Boffetta – I. M. Sokolov “Relative Dispersion in Turbulence”\_DOI: 10.1388/SSC (2003) – PH – 406.
- [5] Lewis Fry Richardson – “Atmospheric Diffusion shown on a Distance-Neighbour Graph” Cambridge University 1925
- [6] Lewis Fry Richardson – “Weather Prediction by Numerical Process”\_CambridgeUniversity\_1922
- [7] P.R. Jonas – “Turbulence and cloud microphysics”\_Atmospheric Research 40 (1996) 283-306
- [8] Dennis Lamb and Johannes Verlinde – “Physics and Chemistry of Clouds” Cambridge University Press\_2011
- [9] Siebert, H.; Franke, H.; Lehmann, K.; Maser, R.; Saw, E.W.; Schell, D.; Shaw, R.A.; Wendisch, M. Probing Finescale – “Dynamics and Microphysics of Clouds with Helicopter-Borne Measurements” Bull. Am. Meteorol. Soc. 2006, 87, 1727–1738.
- [10] Heintzenberg, J. Charlson, R. J. – “Clouds in the Perturbed Climate System: Their Relationship to Energy Balance, Atmospheric Dynamics, and Precipitation” Strüngmann Forum Reports; (Eds.) MIT Press: Cambridge, MA, USA, 2009; ISBN 978-0-262-01287-4

- [11] W. M. Organization. (). International Cloud Atlas, [Online]. Available: <https://cloudatlas.wmo.int/en/clouds-definitions.html>.
- [12] A. M. Society. (). Glossary of Meteorology (June 2000): Relative Humidity. Available:[https://web.archive.org/web/20110707113357/http://amsglossary.allenpress.com/glossary/search-query,relative,humidity&submit\\_2011](https://web.archive.org/web/20110707113357/http://amsglossary.allenpress.com/glossary/search-query,relative,humidity&submit_2011)
- [13] DAVID TOPPING AND GORDON MCFIGGANS Centre for Atmospheric Science, Simon Building, Oxford Road, Manchester
- [14] Wojciech W. Grabowski and Lois Thomas – “Cloud droplet diffusional growth in homogeneous isotropic turbulence”
- [15] Xiang Zhong, Shaw Chen Liu, Run Liu, Xinlu Wang, Jiajia Mo, and Yanzi Li – “Observed trends in clouds and precipitation (1983–2009): implications for their causes”
- [16] Wojciech W. Grabowski and Lois Thomas - Cloud droplet diffusional growth in homogeneous isotropic turbulence. *Atmos. Chem. Phys.*, 21, 4059–4077, 2021 <https://doi.org/10.5194/acp-21-4059-2021>
- [17] Wojciech W. Grabowski and Lian-Ping Wang – Growth of Cloud Droplets in a Turbulent Environment”\_Annual-Reviews-Fluid-Mechanics-2013
- [18] H. Pruppacher and J. Klett – “Microphysics of Clouds and Precipitation”\_Springer Science-Business Media B.V., 2010, ISBN: 978-0-7923-4211-3
- [19] Beard and Ochs – “Warm Rain Initiation: An Overview of Microphysical Mechanisms”, *Journal of Applied Meteorology*, vol. 32, pp. 608–625, 1993.
- [20] B. Devenish, P. Bartello, J. Brenguier, L. Collins, W. Grabowski, R. IJzermans, S. Malinowski, M. Reeks, J. Vassilicos, L. Wang, and Z. Warhaft – “Droplet growth in warm turbulent clouds”, *Q. J. R. Meteorol. Soc.*, vol. 138, pp. 1401–1429, 2012.

- [21] M. Pinsky and A. .Khain – “Fine structure of cloud droplet concentration as seen from the Fast-FSSP measurements. Part I: Method of analysis and preliminary results”, *J. Appl. Met.*, vol. 40, pp. 1515–1537.
- [22] Adrian Tompkins – “Atmospheric Physics” – ICTP
- [23] J. Warner – “The Microstructure of Cumulus Cloud. Part I. General Features of the Droplet Spectrum”, *J. Atmos. Sci*, vol. 26, pp. 1049–1059, 1969.
- [24] H. Siebert, R. A. Shaw, J. Ditas, T. Schmeissner, S. P. Malinowski, E. Bodenschatz, and H. Xu – “High-resolution measurement of cloud microphysics and turbulence at a mountaintop station”\_ *Atmospheric-Measurement-Techniques*
- [25] J. Brenguier – “Observations of cloud microstructure at the centimeter scale”\_ *J. Appl. Meteorol.*, vol. 32, pp. 783–793, 1993.
- [26] E. Bodenschatz, S. Malinowski, R. Shaw, and F. Stratmann – “Can we understand clouds without turbulence?”, *American Association for the Advancement of Science*, vol. 327, pp. 970–971, 2010.
- [27] H. Siebert, S. Gerashenko, A. Gylfason, K. Lehmann, L. R. Collins, R. A. Shaw, and Z. Warhaft – “Towards understanding the role of turbulence on droplets in clouds: In situ laboratory measurements”, *Atmospheric Research*, vol. 97, pp. 426–437, 2010.
- [28] P. Vaillancourt, M. Yau, P. Bartello, and W. Grabowski – “Microscopic approach to cloud droplet growth by condensation. Part II: Turbulence, clustering, and condensational growth”, *J. Atmos. Sci*, vol. 59, pp. 3421–3435, 2002.

- [29] Y. Zhou, A. Wexler, and L. Wang – “Modelling turbulent collision of bi-disperse inertial particles”, *J. Fluid Mech*, vol. 433, pp. 77–104, 2001.
- [30] M. R. Maxey and J. J. Riley – “Equation of motion for a small rigid sphere in a nonuniform flow”, *Phys. Fluids*, vol. 26, p. 883, 1983.
- [31] P. Dimotakis – “Turbulent mixing”, *Annual-Reviews-Fluid-Mechanics*, vol. 37, pp. 329–356, 2005.
- [32] Mark Pinsky and Alexander Khain – “Theoretical Analysis of the Entrainment–Mixing Process at Cloud Boundaries. Part II: Motion of Cloud Interface”.
- [33] J. Westerweel, C. Fukushima, J. M. Pedersen, and J. Hunt – “Momentum and scalar transport at the turbulent/non-turbulent interface of a jet”, *J. Fluid Mech.*, vol. 631, pp. 199–230, 2009.
- [34] J. Brenguier and W. Grabowski – “Cumulus entrainment and cloud droplet spectra: a numerical model within a two-dimensional dynamical framework”, *J. Atmos. Sci.*, vol. 50, pp. 120–136, 1993.
- [35] Paredes Quintanilla, M.E.; Abdunabiev, S.; Allegretti, M.; Merlone, A.; Musacchio, C.; Pasero, E.G.A.; Tordella, D.; Canavero, F. – “Innovative Mini Ultralight Radioprobes to Track Lagrangian Turbulence Fluctuations within Warm Clouds”: *Electronic Design. Sensors* 2021, 21, 1351. <https://doi.org/10.3390/s21041351>.
- [36] Siebert, H.; Franke, H.; Lehmann, K.; Maser, R.; Saw, E.W.; Schell, D.; Shaw, R.A.; Wendisch, M. – “Probing Finescale Dynamics and Microphysics of Clouds

- with Helicopter-Borne Measurements”, *Bull. Am. Meteorol. Soc.* 2006, 87, 1727–1738.
- [37] Heintzenberg, J.; Charlson, R.J. – “Clouds in the Perturbed Climate System: Their Relationship to Energy Balance, Atmospheric Dynamics, and Precipitation”; Strüngmann Forum Reports; (Eds.) MIT Press: Cambridge, MA, USA, 2009; ISBN 978-0-262-01287-4.
- [38] MacPherson, J. I. ; Isaac, G. A. – “Turbulent Characteristics of Some Canadian Cumulus Clouds”. *J. Appl. Meteorol. Climatol.* 1977, 16, 81–90.
- [39] S. Businger, R. Johnson, and R. Talbot – “Scientific Insights from Four Generations of Lagrangian Smart Ballon”, *Atmospheric Research*, vol. 87, pp. 1539–1554, 2006.
- [40] M. Paredes, S. Bertoldo, C. Lucianaz, and M. Allegretti – “Ultra-light disposable radio probes for atmospheric monitoring”, *EGU General Assembly Conference Abstracts*, vol. 20, p. 1389, 2018.
- [41] CLOUD-MyPhyTuTel – “Ideas concerning ultra-light radiosondes”, 2014.
- [42] T. Basso, G. Perotto, C. Musacchio, A. Merlone, A. Athanassiou, and D. Tordella, “Evaluation of Mater Bi Polyactic Acid as materials for biodegradable innovative mini-radiosondes to track small scale fluctuations within clouds”, *Materials Chemistry and Physics*, vol. 253, p. 123 411, 2020.
- [43] M. Paredes – “COMPLETE Workshop: Data and model integration in fluid mechanics”, Imperial College London, December 17 - 19 2019.

- [44] [https://www.bosch\\_sensortec.com/media/boschsensortec/downloads/datasheets/bst-bme280-ds002.pdf](https://www.bosch_sensortec.com/media/boschsensortec/downloads/datasheets/bst-bme280-ds002.pdf).
- [45] A. Wixted, P. Kinnaird, H. Larijani, A. Tait, A. Ahmadiania, and N. Strachan, “Evaluation of LoRa and LoRawan for wireless sensor networks”, 2016 IEEE SENSORS, pp. 1–3, 2016.
- [46] Augustin, A. ; Yi, J. ; Clausen, T. ; Townsley, W. – “A Study of LoRa: Long Range & Low Power Networks for the Internet of Things”. Sensors 2016, 16, 1466.